

# Trust-Region Based Return Mapping Algorithm for Implicit Integration of Elastic-Plastic Constitutive Models

B. T. Lester\* and W. M. Scherzinger

*Solid Mechanics Department, Sandia National Laboratories, Albuquerque, NM 87185, USA*

## SUMMARY

A new method for the solution of the non-linear equations forming the core of constitutive model integration is proposed. Specifically, the trust-region method that has been developed in the numerical optimization community is successfully modified for use in the implicit integration of elastic-plastic models. To this end, the non-quadratic Hosford yield surface is used as a representative case to investigate computationally challenging constitutive models. The theory and implementation are presented, discussed, and compared to other common integration schemes. Multiple boundary value problems are studied and used to verify the proposed algorithm and demonstrate the enabling capabilities of this approach over more common methodologies. Robustness and speed are then investigated and compared to existing algorithms. Through these efforts, it is shown that the utilization of a trust-region approach leads to superior performance versus a traditional closest-point projection Newton-Raphson method and comparable speed and robustness to a line search augmented scheme. Copyright © 0000 John Wiley & Sons, Ltd.

Received ...

**KEY WORDS:** Constitutive Model Integration; Return Mapping Algorithms; Trust-Region; Hosford Yield Surface

## 1. INTRODUCTION

As the phenomenological theory of plasticity has matured in recent decades, the corresponding models being proposed have grown increasingly complex. For instance, non-quadratic yield surfaces like those put forth by Hosford [1], the classical anisotropic form of Hill [2], and more recent models that are both non-quadratic and anisotropic (*i.e.* Barlat and coworkers [3, 4], Karafillis and Boyce [5], and Cazacu and colleagues [6, 7]) have all been developed and implemented. The additional capabilities provided by such models have been useful in the analysis of sheet metal forming [8, 9, 10] and inflation/burst of tubes [11, 12, 13] in which accurately capturing the anisotropic plastic flow is essential.

Similar to the aforementioned plasticity models, structural analyses and corresponding simulations have also grown in terms of complexity and size. In turn, there is an increasing focus on the efficient implicit integration of both the global finite element problem and local stress updating procedure. With respect to the latter constitutive problem, the fully implicit closest point projection (CPP) and semi-implicit convex cutting plane (CCP) return mapping algorithms (RMAs) popularized by Simo, Ortiz, and coworkers [14, 15, 16, 17, 18, 19] have been extensively explored. Such implementations have been pursued for a wide variety of phenomenological constitutive models incorporating a large series of physics and flow rules (*e.g.* [20, 21, 22, 23, 24, 25]). A different approach has been taken by Yoon *et al.* [26, 27, 8], who have proposed a return mapping

\*Correspondence to: btleste@sandia.gov

scheme based on the control of a potential residual. In all of these cases, the Newton-Raphson method is used to solve the non-linear equations forming the core of the stress updating approaches.

Unlike the radial return approaches common with  $J_2$  plasticity, pure Newton-Raphson solvers are not guaranteed to converge for more complex models. Comprehensive studies by Pérez-Foguet and Armero [28] and Scherzinger [29] have extensively explored this issue for a variety of models and demonstrated the insufficiency of a Newton-Raphson solver under many conditions. For implicit global solvers, the ability of the constitutive routine to converge under any input deformation is important to avoid costly cutbacks to the global timestep. This is especially true for non-linear, large-deformation finite element codes like Sierra/SM [30, 31, 32] that utilize an iterative global solver and therefore may see a wider range of trial deformations during the solution process.

To improve the convergence properties, a variety of modifications to the underlying algorithms have been proposed. One of the more common approaches is to break up large input deformations into a series of smaller loadings and sequentially solve the subloadings until the intended total deformation is achieved. Although more common with explicit integration schemes, these substepping approaches have been adopted by Yoon and colleagues [26, 27, 8], Seifert *et al.* [33, 34], and Rabahallah and coworkers [35] for a wide variety of constitutive models. Such methods, however, mitigate some of the advantages of a fully implicit scheme and introduce additional complexity to the ensuing implementation. An alternative to this has been the adoption of more complex numerical schemes to ensure convergence – notably line search methods. Early works like those of Dutko *et al.* [36] observed improvements in adding an additional line search step while more recent efforts such as those by Seifert and coworkers [37], Pérez-Foguet and Armero [28], and Scherzinger [29] have all extensively explored and demonstrated these benefits. For instance, Scherzinger noted convergence of the line search augmented CPP method for any trial stresses whose effective measure was less than or equal to 30 times that of yield for both the Hosford and Barlat models [29] – far exceeding the performance of a pure Newton-Raphson solver.

These previous efforts (substepping and line search schemes) have focused on modifying or augmenting the Newton-Raphson solver to improve robustness. Given the developments in non-linear optimization and numerical methods since the early efforts of Simo, Ortiz, Hughes, and others, an alternative approach to consider is the utilization of a new solver scheme with the CPP-RMA problem. One such possibility are *trust-region* based methods [38]. At their core, these algorithms search for updated solution variables minimizing an objective function within a trusted solution variable domain. Although primarily studied for general optimization problems [39, 40, 41, 42, 43], trust-region methods have been successfully adopted in structural design optimization [44] and flow control [45] applications. A previous effort by Shterenlikht and Alexander [46] attempted to use open-source implementations of both Levenberg-Marquardt and dogleg trust-region methods to integrate the Gurson-Tvergaard-Needleman (GTN) model. In their investigation, the former approach showed promise while severe issues with scaling were encountered with the latter leading to substantial convergence difficulty.

In this work, the possibility of using a tailored trust-region approach for the CPP-RMA problem to integrate elastic-plastic constitutive models is explored. Specifically, the numerical formulation of a Hosford plasticity model using a trust-region solution method is developed and implemented. A series of boundary value problems are then investigated to demonstrate the capabilities of this novel methodology and investigate the performance characteristics (especially convergence) in comparison to established Newton-Raphson and line search augmented approaches. To this end, this work is organized as follows. Section 2 describes the elastic-plastic model and its numerical implementation. Both the theoretical formulation and some basic discussion of the three solution methods – Newton-Raphson (NR), line search augmented Newton-Raphson (LS-NR), and the trust-region approach (TR) – is presented along with details of the trust-region implementation. Numerical results and discussion are presented in Section 3 while concluding remarks are given in Section 4.

## 2. TRUST-REGION IMPLEMENTATION OF ELASTIC-PLASTIC MODELS

To investigate trust-region based constitutive model integration, a numerical implementation of the Hosford model [1] is developed. This selection is made as it is a relatively simple form (only two parameters and isotropic) while still being able to induce substantial curvature in the yield surface. It is noted that the algorithm is presented in a sufficiently general fashion so that it is easily adaptable for use with other yield surfaces or isotropic hardening laws<sup>†</sup>. The theoretical model is presented in the next section while the numerical implementation is presented in Section 2.2.

### 2.1. Hosford Plasticity Model

Like many other elastic-plastic models, an additive split in the strain tensor is assumed such that,

$$\varepsilon_{ij} = \varepsilon_{ij}^e + \varepsilon_{ij}^p \quad (1)$$

where  $\varepsilon_{ij}$ ,  $\varepsilon_{ij}^e$ , and  $\varepsilon_{ij}^p$  are the total, elastic, and plastic strain tensors, respectively. The symmetric Cauchy stress,  $\sigma_{ij}$ , is given as,

$$\sigma_{ij} = \mathbb{C}_{ijkl} \varepsilon_{kl}^e = \mathbb{C}_{ijkl} (\varepsilon_{kl} - \varepsilon_{kl}^p), \quad (2)$$

with  $\mathbb{C}_{ijkl}$  being the fourth order elastic stiffness tensor (assumed isotropic). This leads to a stress rate equation<sup>‡</sup> of the form,

$$\dot{\sigma}_{ij} = \mathbb{C}_{ijkl} (\dot{\varepsilon}_{kl} - \dot{\varepsilon}_{kl}^p). \quad (3)$$

Assuming an associative flow rule the rate of plastic strain,  $\dot{\varepsilon}_{ij}^p$ , can be written as

$$\dot{\varepsilon}_{ij}^p = \dot{\gamma} \frac{\partial f}{\partial \sigma_{ij}}, \quad (4)$$

where  $\dot{\gamma}$  is the plastic consistency multiplier and  $f$  is the yield function describing the domain of elastic deformation. The plastic multiplier is found through consistency relations resulting from the traditional Kuhn-Tucker conditions,

$$\dot{\gamma} \geq 0; \quad \dot{\gamma} f = 0; \quad f \leq 0. \quad (5)$$

Bearing this in mind, the response of the model is largely dictated by the yield surface and hardening rule considered. In this case, the yield function is given by

$$f(\sigma_{ij}, \bar{\varepsilon}^p) = \phi(\sigma_{ij}) - \sigma_y(\bar{\varepsilon}^p) \quad (6)$$

where  $\sigma_y$  is the yield stress,  $\bar{\varepsilon}^p$  is the isotropic hardening variable (equivalent plastic strain) and  $\phi$  is the Hosford effective stress [1] defined as

$$\phi(\sigma_{ij}) = \left[ \frac{|\sigma_1 - \sigma_2|^a + |\sigma_2 - \sigma_3|^a + |\sigma_1 - \sigma_3|^a}{2} \right]^{1/a}, \quad (7)$$

with  $\sigma_i$  being the principal stresses and  $a$  the fitting exponent ( $1 \leq a \leq \infty$ ) giving the model its non-quadratic nature. In the developed algorithm, the numerical routine put forth by Scherzinger and Dohrmann [49] is used to determine the principal stresses. Linear hardening of the form,

$$\sigma_y(\bar{\varepsilon}^p) = \sigma_y^0 + K \bar{\varepsilon}^p, \quad (8)$$

<sup>†</sup>Kinematic hardening is not treated in this work although the authors see no reason that would preclude an extension to such models.

<sup>‡</sup>As the focus of this effort is on numerical methods for solving local constitutive relations, discussions towards objective stress rates are neglected. For details and discussions of such issues, the reader is referred to [47, 48, 23, 33].

is considered in which  $\sigma_y^0$  is a constant initial yield stress and  $K$  the hardening modulus. Additionally, for this study it is assumed that the loadings are isothermal and temperature dependence is neglected. Details of this model, notably the derivatives of the effective stress, may be found in the previous work of Scherzinger [29].

## 2.2. Numerical Implementation

Regardless of numerical solution scheme (NR, LS-NR, or TR), the underlying non-linear stress updating problem is the same. Specifically, to numerically integrate the hypoelastic constitutive response posed in Section 2.1, an elastic predictor-inelastic corrector scheme based on operator splitting [14] is adopted. By assuming the given loading increment does not lead to inelastic deformation, an elastic trial stress,  $\sigma_{ij}^{\text{tr}}$ , is computed as,

$$\sigma_{ij}^{\text{tr}} = \sigma_{ij}^{(n)} + \mathbb{C}_{ijkl} d\varepsilon_{kl}^{(n+1)} \quad (9)$$

with the superscripts “ $(n)$ ” and “ $(n+1)$ ” referring to variables at those load steps and  $d\varepsilon_{ij}$  is the total strain increment. The validity of the elastic step may be determined by computing  $f^{\text{tr}} = f(\sigma_{ij}^{\text{tr}}, \bar{\varepsilon}^{p(n)})$ . If  $f^{\text{tr}} < 0$ , the elastic step is valid and the state variables are updated ( $\sigma_{ij}^{(n+1)} = \sigma_{ij}^{\text{tr}}$ ,  $\bar{\varepsilon}^{p(n+1)} = \bar{\varepsilon}^{p(n)}$ ). The much more interesting plastic loading case occurs when  $f^{\text{tr}} > 0$ .

The solution to the inelastic correction is associated with the constrained optimization problem corresponding to maximum dissipation – see [36, 19, 50, 51, 25] for discussions on the thermodynamics. During the inelastic correction, the solution is found by iteratively refining the state variables and returning to the yield surface. For implicit methods like the CPP approach pursued here, this process is performed by enforcing the consistency relation and the plastic strain flow rule on the material state at  $t = t_{n+1}$ . Mathematically, these two conditions are given in residual form as

$$r_I^{(n+1)}(x_I^{(n+1)}) = \begin{Bmatrix} r_{ij}^{\varepsilon(n+1)} \\ r_f^{(n+1)} \end{Bmatrix} = \begin{Bmatrix} -d\varepsilon_{ij}^{p(n+1)} + d\gamma^{(n+1)} \frac{\partial\phi}{\partial\sigma_{ij}^{(n+1)}} \\ f(\sigma_{ij}^{(n+1)}, d\gamma^{(n+1)}) \end{Bmatrix} = \begin{Bmatrix} 0 \\ 0 \end{Bmatrix}, \quad (10)$$

where  $x_I$  are the solution variables that may be written as,

$$x_I^{(n+1)} = \begin{bmatrix} \sigma_{ij}^{(n+1)} \\ d\gamma^{(n+1)} \end{bmatrix}. \quad (11)$$

The first residual,  $r_{ij}^{\varepsilon}$ , is associated with the flow rule while the second,  $r_f$ , is the consistency condition.<sup>§</sup>

The non-linear problem posed by  $r_I = 0$  is solved numerically by iterating until convergence has been achieved. In this work, a merit function of the form,

$$\psi(x_I) = \frac{1}{2} D_{JK}^1 r_K(x_I) D_{JL}^1 r_L(x_I) \quad (12)$$

in which  $D_{IJ}^1$  is a constant, diagonal matrix taking the form,

$$D_{IJ}^1 = \begin{bmatrix} c^{\varepsilon} \mathbb{I}_{ijkl} & 0_{ij} \\ 0_{ij} & c^f \end{bmatrix}, \quad (13)$$

where  $\mathbb{I}_{ijkl}$  is the fourth order identity tensor, is used to assess convergence. Specifically, the square root of the merit function ( $\sqrt{\psi}$ ) is used as the convergence criteria. Essentially, these constants are

<sup>§</sup>In what follows, capital subscript indices will be used to refer to elements of larger matrices and vectors that may be either scalar or tensor. Traditional summation conventions over an abbreviated interval ( $I = 1, 2$ ) will be used to indicate operations between these larger matrix and vector objects while lower case indices shall be reserved for individual tensor components.

introduced as weights to appropriately scale the contributions of the different components of the residual. From Eqn. 10 it is noted that in the residual and solution variable vectors, both strain and stress quantities are evident. Depending on the units being used, the difference in the values of the variables can be many orders of magnitude, highlighting the necessity of appropriately normalizing the problem. Importantly, regardless of the the values of  $c^\varepsilon$  and  $c^f$  the minimum is achieved at  $r_{ij}^\varepsilon = r^f = 0$ . By setting the constants to be one,  $D_{IJ}^1$  reduces to the identity matrix and the more traditional merit function of the form  $\psi = (1/2) r_I r_I$  is recovered. Trust-region methods, however, are more susceptible to scaling issues as experienced by Shterenlikht and Alexander [46]. In the remainder of this work, an equal weight, stress-normalization is introduced by setting  $c^\varepsilon = E/\sigma_y^0$  and  $c^f = 1/\sigma_y^0$  such that the merit function may be written as,

$$\psi(r_I) = \frac{1}{2} \left( \left( \frac{E}{\sigma_y^0} \right)^2 r_{ij}^\varepsilon r_{ij}^\varepsilon + \left( \frac{r^f}{\sigma_y^0} \right)^2 \right). \quad (14)$$

The impact of this scaling on the algorithm performance is explored in Section 3.3.

To begin the inelastic correction process, the state variable values at the  $k = 0$  iteration are initialized to those of the trial state and  $d\varepsilon_{ij}^{p(k=0)} = d\gamma^{(k=0)} = 0$ .<sup>¶</sup> For all three numerical solution schemes considered here, the solution variables are iteratively updated via

$$x_I^{(k+1)} = x_I^{(k)} + \alpha^{(k)} p_I^{(k)}, \quad (15)$$

where  $\alpha^{(k)}$  and  $p_I^{(k)}$  are the step size and vector, respectively, and  $p_I = [p_{ij}^\sigma, p^\gamma]^T$  with  $p_{ij}^\sigma = \Delta\sigma_{ij}$  and  $p^\gamma = \Delta\gamma$ . The three approaches (NR, LS-NR, and TR) differ in how the step size,  $\alpha^{(k)}$ , and step vector,  $p_I^{(k)}$  are determined.

In the simplest and most-common approach (NR), the step size is fixed ( $\alpha^{(k)} = 1$ ) and the step vector,  $p_I^{NR(k)}$ , takes the classical form of,

$$p_I^{NR(k)} = - \left( J^{(k)} \right)_{IJ}^{-1} r_J^{(k)} \quad (16)$$

with  $J_{IJ}$  being the Jacobian defined as  $J_{IJ} = \frac{\partial r_I}{\partial x_J}$ . Given the residuals in Eqn. 10, the Jacobian is

$$J_{IJ} = \begin{bmatrix} (\mathcal{L}_{ijkl})^{-1} & \frac{\partial \phi}{\partial \sigma_{ij}} \\ \frac{\partial \phi}{\partial \sigma_{ij}} & -\frac{\partial \sigma_y}{\partial \varepsilon^p} \end{bmatrix}, \quad (17)$$

where  $\mathcal{L}_{ijkl}$  is given by,

$$\mathcal{L}_{ijkl} = \left( \mathbb{C}_{ijkl}^{-1} + d\gamma \frac{\partial^2 \phi}{\partial \sigma_{ij} \partial \sigma_{kl}} \right)^{-1}. \quad (18)$$

Line search approaches vary from NR and other methods by selecting a step direction (in this case, the NR direction) and then finding a step size minimizing the merit function in the domain  $\alpha^{(k)} = (0, 1]$ . This constraint serves to enforce that each iteration reduces the merit function. As an exact minimum can be expensive to compute, an approximate minimum is found by a quadratic approximation. In practice, the utilization of a LS approach is fairly straight-forward as it only requires an additional step to find  $\alpha^{(k)}$ . For details of the implemented LS-NR scheme for the Hosford model, see the work of Scherzinger [29].

Unlike line search methods that directly investigate the merit function, trust-region based schemes instead construct a local approximation via a model problem,  $m^{(k)}$  ( $p_I$ ), and find the step vector that

<sup>¶</sup>In the remainder of this section, it shall be assumed that unless specifically noted the variable values correspond to those at the “ $(n + 1)$ ” timestep and “ $(k)$ ” and “ $(k + 1)$ ” superscripts are to denote the previous and current correction iterations. Furthermore, the term increment shall be reserved for use with the global time/loadstep while iteration shall be used to describe the inelastic correction process.

minimizes the model problem. As this representation is only an approximation of the actual non-linear problem, the step vector is only found in the space sufficiently close to the current solution that can be trusted (hence the name). This domain is defined to be the region in solution variable space within a ball of radius  $\Delta^{(k)}$  ( $\|p_I^{(k)}\| \leq \Delta^{(k)}$ ). The size of this trust-region is then updated depending on the improvement (or lack thereof) of a guess step vector. Limiting the solution space serves to highlight a key distinction between line search and trust-region methods. Namely, the latter first picks a step size and then finds the step vector. [38]

In the current study, a quadratic approximation of the form [38],

$$m^{(k)}(p_I) = \Psi^{(k)} + g_I^{(k)} p_I + \frac{1}{2} p_I B_{IJ}^{(k)} p_J, \quad (19)$$

is used for the model problem where  $\Psi^{(k)}$  is the function to be minimized,  $g_I^{(k)}$  is the gradient of  $\Psi^{(k)}$  ( $\nabla \Psi_I^{(k)}$ ), and  $B_{IJ}^{(k)}$  is an approximation of the Hessian ( $\nabla^2 \Psi_{IJ}^{(k)}$ ). When  $\Psi^{(k)}$  is an unweighted form of Eqn. 12 ( $c^e = c^f = 1$ ), these terms are commonly written as,

$$\Psi^{(k)} = \frac{1}{2} r_I^{(k)} r_I^{(k)}; \quad g_I^{(k)} = J_{JI}^{(k)} r_J^{(k)}; \quad B_{IJ}^{(k)} = J_{LI}^{(k)} J_{LJ}^{(k)}. \quad (20)$$

Schematically, this method is illustrated in Fig. 1 in which a simplified case of  $J_2$  plasticity with no hardening is treated. In this case, contours corresponding to a representative model problem,  $m^{(k)}$ , (whose chosen form is selected for demonstration purposes) are presented alongside the yield surface and initial and final stress states. Two circles of radii  $\Delta^1$  and  $\Delta^2$  corresponding to different domains along with their minimization vectors,  $p_I^1$  and  $p_I^2$ , are also presented. In this realization, the contributions of the effective plastic strain on the trust-region size,  $\Delta^{(k)}$ , are neglected for clarity of presentation. Importantly, as is observed from Fig. 1, it is noted that by changing the trust-region radius from  $\Delta^1$  to  $\Delta^2$  not only changes the magnitude of the step direction vectors ( $p_I^1$  and  $p_I^2$ ) but also the direction highlighting the impact of this parameter. Successive iterations adjust the size of the trust-region based on measures of improvement and algorithmic rules. A corresponding refined model problem is also produced that is then minimized over the next iteration. Through this iterative process, the material state converges on the correct solution.

As mentioned earlier, variable scaling may substantially affect convergence for the non-linear problem corresponding to constitutive model integration and needs to be handled appropriately. One common way to deal with this is to introduce the scaling ahead of time and develop a modified model problem,  $\tilde{m}^{(k)}$ , that is of the general form given in Eqn. 19 [38]. In this way, the contributions of the different solution variables equally contribute and all of the developments towards solving the problems posed by Eqns. 19 and 20 can be leveraged.

To come up with the scaled model problem,  $\tilde{m}^{(k)}$ , two areas need to be addressed. The first has already been discussed in this section – the merit function. Specifically, the merit function serves as the function to be minimized such that  $\psi^{(k)}$  plays the role of  $\Psi^{(k)}$  in the scaled problem. The second scaling issue that needs to be addressed is associated with the differences in the solution variables and is manifest in the step vector,  $p_I^{(k)}$ . A similar approach to that of the merit function is used and a scaled step vector,  $\tilde{p}_I^{(k)}$ , is introduced such that,

$$\tilde{p}_I^{(k)} = D_{IJ}^2 p_J^{(k)}, \quad (21)$$

with  $D_{IJ}^2$  taking the form,

$$D_{IJ}^2 = \begin{bmatrix} b^\sigma \mathbb{I}_{ijkl} & 0_{ij} \\ 0_{ij} & b^\gamma \end{bmatrix}. \quad (22)$$

A scaled trust-region magnitude,  $\tilde{\Delta}^{(k)}$ , is also introduced such that  $\|\tilde{p}_I^{(k)}\| \leq \tilde{\Delta}^{(k)}$ . For these scalings, a stress normalization is again used such that  $b^\sigma = 1$  and  $b^\gamma = 2\mu$ . By using  $\psi^{(k)}$  as the merit function and using Eqn. 21 to write the scaled model problem,  $\tilde{m}^{(k)}$ , in terms of the scaled step vector produces an expression of the form,

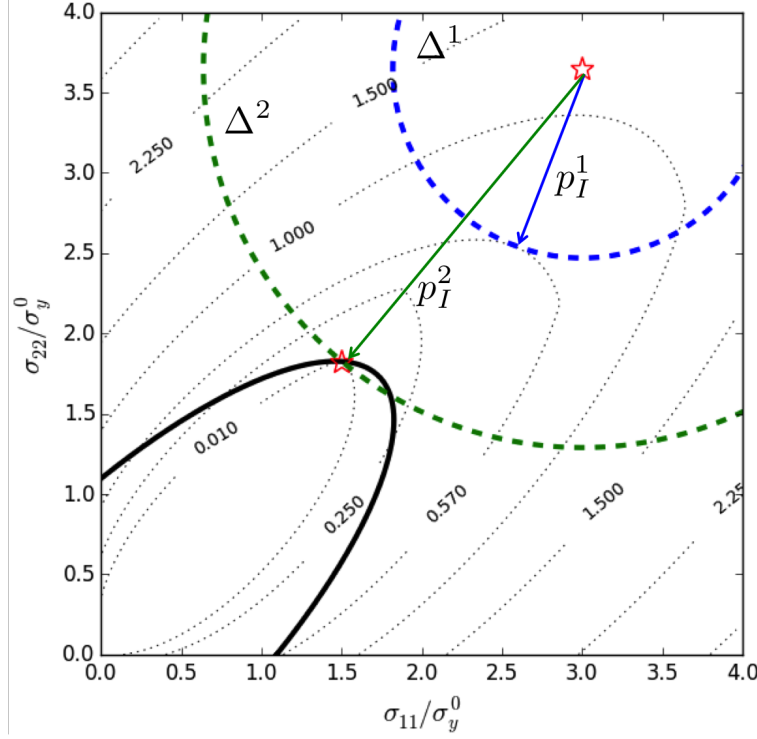


Figure 1. Schematic representation of the TR correction approach. A  $J_2$  yield surface (solid black line) is marked along with an initial and final stress state (red stars). Dotted black lines correspond to the contours of a representative model problem,  $m^{(k)}$ . Two different trust-region domains (and their radii,  $\Delta^{1,2}$ ) are marked along with the corresponding step direction vector,  $p_I^{1,2}$ .

$$\tilde{m}^{(k)}(\tilde{p}_I) = \psi^{(k)} + \tilde{g}_I^{(k)}\tilde{p}_I + \frac{1}{2}\tilde{p}_I\tilde{B}_{IJ}^{(k)}\tilde{p}_J, \quad (23)$$

where the introduction of  $\tilde{p}_I$  leads to the following relation for the gradient,

$$\tilde{g}_I^{(k)} = D_{LK}^1 r_K^{(k)} D_{LJ}^1 J_{JN}^{(k)} (D^2)_{NI}^{-1}, \quad (24)$$

and Hessian,

$$\tilde{B}_{IJ}^{(k)} = (D^2)_{IL}^{-1} D_{MK}^1 J_{KN}^{(k)} D_{MA}^1 J_{AL}^{(k)} (D^2)_{NJ}^{-1}, \quad (25)$$

terms, respectively. More convenient forms of these expressions may be written,

$$\tilde{g}_I^k = \left[ \frac{(c^\varepsilon)^2}{b^\sigma} r_{kl}^{\varepsilon(k)} \mathcal{L}_{kl}^{-1} + \frac{(c^f)^2}{b^\sigma} r^{f(k)} \frac{\partial \phi}{\partial \sigma_{ij}^{(k)}}, \quad \frac{(c^\varepsilon)^2}{b^\gamma} r_{ij}^{\varepsilon(k)} \frac{\partial \phi}{\sigma_{ij}^{(k)}} - \frac{(c^f)^2}{b^\gamma} r^{f(k)} \frac{\partial \sigma_y}{\partial \bar{\varepsilon}^{p(k)}} \right]^T, \quad (26)$$

and,

$$\tilde{B}_{IJ}^k = \left[ \begin{array}{cc} \left(\frac{c^\varepsilon}{b^\sigma}\right)^2 \mathcal{L}_{ijrs}^{-1} \mathcal{L}_{rskl}^{-1} + \left(\frac{c^f}{b^\sigma}\right)^2 \frac{\partial \phi}{\partial \sigma_{ij}^{(k)}} \frac{\partial \phi}{\partial \sigma_{kl}^{(k)}}, & \frac{(c^\varepsilon)^2}{b^\sigma b^\gamma} \mathcal{L}_{ijrs}^{-1} \frac{\partial \phi}{\partial \sigma_{rs}^{(k)}} - \frac{(c^f)^2}{b^\sigma b^\gamma} \frac{\partial \sigma_y}{\partial \bar{\varepsilon}^{p(k)}} \frac{\partial \phi}{\partial \sigma_{ij}^{(k)}} \\ \frac{(c^\varepsilon)^2}{b^\sigma b^\gamma} \mathcal{L}_{klrs}^{-1} \frac{\partial \phi}{\partial \sigma_{rs}^{(k)}} - \frac{(c^f)^2}{b^\sigma b^\gamma} \frac{\partial \sigma_y}{\partial \bar{\varepsilon}^{p(k)}} \frac{\partial \phi}{\partial \sigma_{kl}^{(k)}}, & \left(\frac{c^\varepsilon}{b^\gamma}\right)^2 \frac{\partial \phi}{\partial \sigma_{rs}^{(k)}} \frac{\partial \phi}{\partial \sigma_{rs}^{(k)}} + \left(\frac{c^f}{b^\gamma}\right)^2 \frac{\partial \sigma_y}{\partial \bar{\varepsilon}^{p(k)}} \frac{\partial \sigma_y}{\partial \bar{\varepsilon}^{p(k)}} \end{array} \right]. \quad (27)$$

Given the scaled model problem, a method to find the desired scaled step vector is needed. The established dogleg method is utilized for this purpose and will be briefly reviewed here. For details and more extensive discussion, please see the text of Nocedal and Wright [38].

In order to iteratively update the solution vector, an initial,  $\bar{\Delta}^0$ , and maximum,  $\bar{\Delta}$ , trust-region radius must first be defined. To this end, it is noted that the proposed algorithm is an incremental constitutive formulation. Therefore, it is expected that (i) the corrected stress tensor must lie between the trial stress and the previously converged stress and (ii) the maximum possible plastic strain increment would be the total strain increment. Therefore, the maximum trust-region radius,  $\bar{\Delta}$ , is set to,

$$\bar{\Delta} = b^\sigma \sqrt{(\sigma_i^{tr} - \sigma_i^n)(\sigma_i^{tr} - \sigma_i^n)} + b^\gamma d\bar{\varepsilon}, \quad (28)$$

where  $\sigma_i^{tr}$  and  $\sigma_i^n$  are the principal components of the corresponding stress states and

$$d\bar{\varepsilon} = \sqrt{\frac{2}{3} d\varepsilon_{ij}^{n+1} d\varepsilon_{ij}^{n+1}}. \quad (29)$$

The initial trust-region radius is selected as  $\bar{\Delta}^0 = \bar{\Delta}$ . Importantly, this selection ensures that if a single step solution exists it may be found.

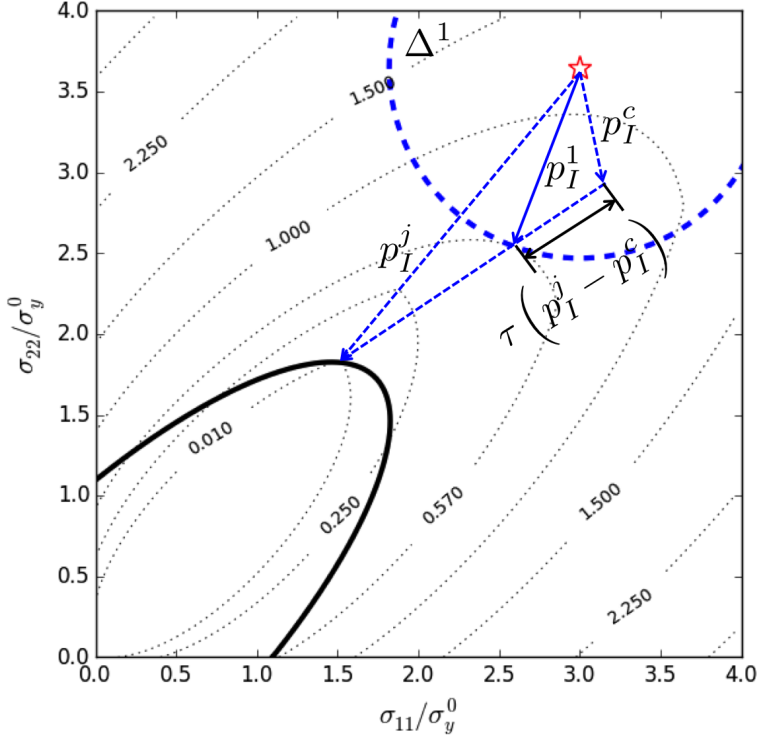


Figure 2. Illustration of the dogleg approximation to find  $p_I^1$  as a combination of the Cauchy point,  $p_I^c$  and full step vectors,  $p_I^j$ .

To iteratively update the scaled step vector,  $\tilde{p}_I^{(k)}$ , and scaled trust-region radius,  $\tilde{\Delta}^{(k)}$ , the aforementioned dogleg method is used. This approach is schematically represented in Fig. 2. Specifically, the dogleg method utilizes two scaled step vectors – the Cauchy point,  $\tilde{p}_I^c$ , and full step,  $\tilde{p}_I^j$  – and finds the point running between them that lies closest to the edge of the trust-region. The former corresponds to the solution of the linear constrained (in terms of solution step magnitude) problem while the latter is the minimizer of the unconstrained quadratic model problem, Eqn. 23, and is essentially a scaled Newton-Raphson step. These vectors are given as,

$$\tilde{p}_I^{c(k)} = -\tau^{(k)} \left( \frac{\tilde{\Delta}^{(k)}}{\|\tilde{g}_I^{(k)}\|} \right) \tilde{g}_I^{(k)}, \quad (30)$$

with  $\tau^{(k)}$  being,

$$\tau^{(k)} = \min \left[ 1, \frac{\|\tilde{g}_I^{(k)}\|^3}{\tilde{\Delta}^{(k)} \tilde{g}_I^{(k)} \tilde{B}_{IJ}^{(k)} \tilde{g}_J^{(k)}} \right], \quad (31)$$

and

$$\tilde{p}_I^{j(k)} = - \left( \tilde{B}^{(k)} \right)_{IJ}^{-1} \tilde{g}_J^{(k)}. \quad (32)$$

If the Cauchy point,  $\tilde{p}_I^{c(k)}$ , lies on the boundary of the trust-region it is accepted as the minimizing step vector. When this condition is not satisfied, a vector running from the current material state (stress state in Fig. 2) to a point lying along the path connecting the Cauchy point and the full step with a magnitude of  $\tilde{\Delta}^{(k)}$  is searched for. If the full step lies within the trust-region it is used. This process is given by Eqn. 33,

$$\begin{aligned} & \text{if } \|\tilde{p}_I^{c(k)}\| = \tilde{\Delta}^{(k)} \\ & \quad \tilde{p}_I^{(k)} = \tilde{p}_I^{c(k)} \\ & \text{else} \\ & \quad \tilde{p}_I^{(k)} = \tilde{p}_I^{c(k)} + \tau \left( \tilde{p}_I^{j(k)} - \tilde{p}_I^{c(k)} \right), \end{aligned} \quad (33)$$

with  $\tau$  being between  $(0, 1]$ . To find  $\tau$ , a simple bisection algorithm is employed in this effort in lieu of more complex approaches that have been adopted (*i.e.* conjugate gradient).

To update the trust-region radius, a measure of the iterative improvement is first determined. Specifically,  $\rho^{(k)}$  is defined as the actual improvement over expected and is given as,

$$\rho^{(k)} = \frac{\psi(x_I^{(k)}) - \psi(x_I^{(k)} + p_I^{(k)})}{\tilde{m}^{(k)}(0) - \tilde{m}^{(k)}(\tilde{p}_I^{(k)})}, \quad (34)$$

and it can be noted that  $\tilde{m}^{(k)}(0) = \psi^{(k)}$ . The updated scaled trust-region radius,  $\tilde{\Delta}^{(k+1)}$ , is determined based on this improvement measure. If substantial improvement is noted, the radius is increased. On the other hand, when unacceptable gains are made the trusted region is reduced in size. The update process is given as,

$$\begin{aligned} & \text{if } \rho^{(k)} < \frac{1}{4} \\ & \quad \tilde{\Delta}^{(k+1)} = \frac{1}{4} \|\tilde{p}_I^{(k)}\|, \\ & \text{else} \\ & \quad \text{if } \rho^{(k)} > \frac{3}{4} \text{ and } \|\tilde{p}_I^{(k)}\| = \tilde{\Delta}^{(k)} \\ & \quad \quad \tilde{\Delta}^{(k+1)} = 2\tilde{\Delta}^{(k)} \\ & \quad \text{else} \\ & \quad \quad \tilde{\Delta}^{(k+1)} = 2\|\tilde{p}_I^{(k)}\| \\ & \quad \tilde{\Delta}^{(k+1)} = \min \left( \tilde{\Delta}^{(k+1)}, \bar{\Delta} \right). \end{aligned} \quad (35)$$

At this stage, an additional check is performed to ensure that the updated solution vector is actually an improvement. Specifically, if  $\rho^{(k)}$  is above a threshold value,  $\rho^{(k)} > \eta = 0.1$ , the solution is considered to be an acceptable improvement. If not, the updated guess is unacceptable and rejected. These conditions for these checks are,

```

if  $\rho^{(k)} > \eta$ 
  Accept Solution  $x_I^{(k+1)} = x_I^{(k)} + p_I^{(k)}$ ,
else
  Reject Solution  $x_I^{(k+1)} = x_I^{(k)}$ ,
  Force  $(k + 1)$  iteration to use the Cauchy step:  $\tilde{p}_I^{(k+1)} = \tilde{p}_I^{c(k+1)}$ .

```

(36)

Note, the updating procedures in Eqns. 35 and 36 largely follow those in Algorithm 11.5 of [38]. Two key differences are evident in the proposed schemes versus that of [38]. The first being that in the event of a rejected step, the subsequent iteration is forced to take a Cauchy step. This is analogous to non-linear conjugate gradient algorithms taking a steepest descent step when unacceptable orthogonality is observed. Furthermore, under acceptable conditions the trust-region radius scales with the step vector magnitude ( $\tilde{\Delta}^{k+1} = 2\|\tilde{p}_I^k\|$ ). These changes were found during algorithm development to improve convergence under numerically challenging conditions and as such are utilized here.

### 3. RESULTS

To investigate the performance of the the model presented in Section 2, it was implemented in the non-linear, quasistatics finite element code Sierra/SM [30, 31, 32]. First, a series of boundary value problems are considered in Section 3.1 to both verify the proposed algorithm and demonstrate its capabilities. The robustness and algorithmic performance are then extensively explored in Section 3.2. In both these cases, the proposed implementation will be compared to those of both a standard NR and a LS-NR algorithm. Finally, in Section 3.3, the impact of the scaling terms in Eqns. 13 and 22 will be explored. For these studies, properties representative of an elastic-plastic metal will be used ( $E = 200$  GPa,  $\nu = 0.3$ ,  $\sigma_y^0 = 200$  MPa).

#### 3.1. Verification Problems

A series of global boundary value problems are solved in this section using the three considered algorithms to verify the TR approach. Previous studies have emphasized the importance of using *consistent* (algorithmic) over *continuum* tangent moduli to maintain the desired rates of convergence at the global level [52, 53]. For the cases studied here, the linearization and differentiation of the plastic flow residual and constitutive equation is the same across the proposed algorithms. The differences between them is associated with the numerical approach to solve the non-linear problem (Eqn. 10) posed by these relations. Therefore, the consistent tangent moduli are the same. Regardless, the Sierra/SM FE code being used to solve the current problems does not require an analytical tangent modulus from the implemented constitutive routines [32] and as such it is not presented. Importantly, these considerations mean that the specification of the tangent modulus does not affect the relative performance of the three schemes studied here. For these verification problems, linear hardening with  $K = 20$  GPa will be considered along with a yield exponent of  $a = 8$  that is common for FCC metals [54].

**3.1.1. Biaxially Loaded Plate** The capabilities of the TR numerical implementation developed in this work are now explored. For these investigations, a thin sheet ( $1 \times 0.5 \times 0.01$  mm length ( $L$ ) by width ( $W$ ) by thickness ( $t$ )) comprised of nine linear hexahedron elements is considered. A set of

six biaxial loadings corresponding to tension, compression, and various mixed conditions as shown in Fig. 3a are imposed along the indicated edges in Fig. 3b and analyzed. Eighth-symmetry, plane stress conditions are assumed for the remaining boundaries and fifty load steps are used for each analysis. The in-plane stress and strain results are presented below in Fig. 4 for the NR, LS-NR, and TR solution methods.

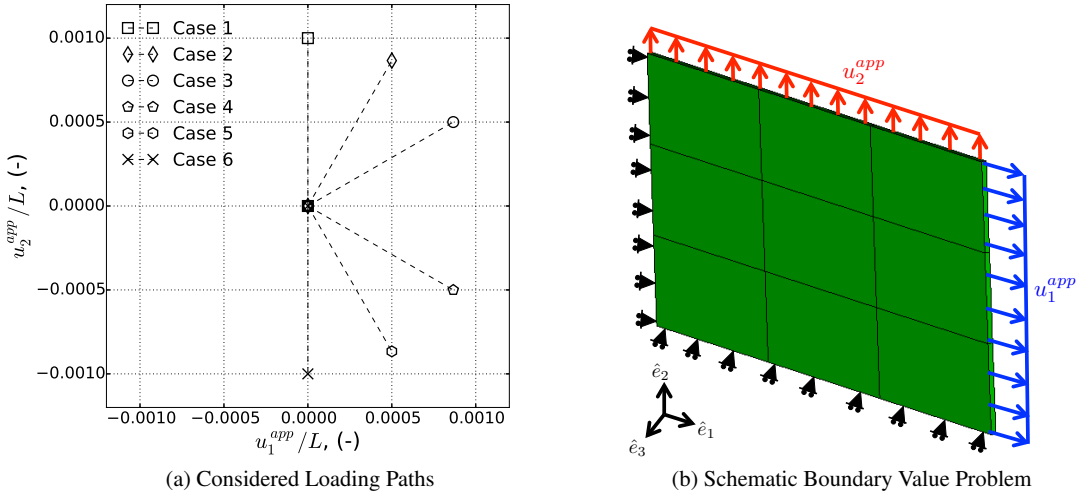


Figure 3. Considered (a) loading paths and (b) boundary value problem for the biaxially loaded plate tests

Excellent agreement between the three different implementations is noted in the six responses of Fig. 4. The maximum relative differences of any of the algorithms was on the order of  $1 \times 10^{-3}\%$  although the error was primarily zero. In this way, the capability of the proposed trust-region model through a variety of simple loading paths is demonstrated. With respect to the speed of the different approaches, Table I presents the relative wallclock time of the different methods to those of the NR approach. This baseline is selected as it represents the most common implicit implementation and the relative cost of going to these more complex methodologies can be ascertained. Each case is run on a single processor of the same dedicated machine to minimize any variability and take just under a second. During plastic loading, two correction iterations are typically needed for each implementation. As can be seen from Table I utilization of the LS-NR or TR methods comes at only a modest cost. For the LS-NR approach, the additional time is less than 4% in all cases. The TR algorithm is typically slower than LS-NR approach but the overall increase in time is still less than 7%.

Case	NR	LS-NR	TR
1	1.000	1.026	1.066
2	1.000	1.024	1.038
3	1.000	1.006	1.014
4	1.000	1.039	1.025
5	1.000	1.021	1.005
6	1.000	1.009	1.038

Table I. Relative (to the NR method) computational times for NR, LS-NR, and TR methods through the six loading paths in Fig. 3a.

**3.1.2. Rod in Combined Tension and Shear** The previous study focused on a relatively simple geometry of limited size. To further test the capabilities of this implementation, the problem of a rod

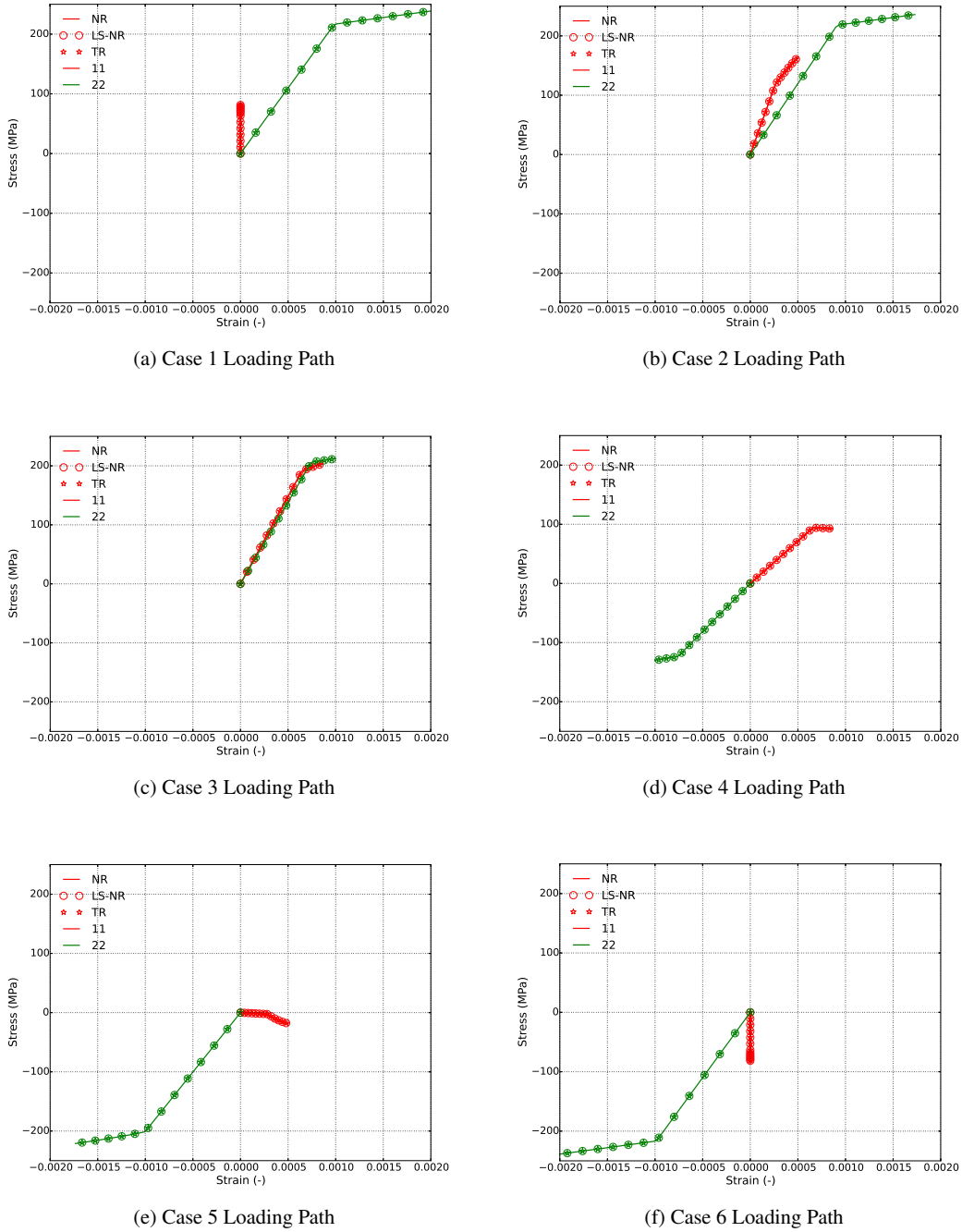


Figure 4. Stress-strain responses in the 11 and 22 directions for the six loading cases presented in Fig. 3a as determined by the NR, LS-NR, and TR methods.

subject to tension and shear previously tackled by Shterenlikht and Alexander [46] is considered. This specific problem is investigated for two reasons. First, as pointed out by Shterenlikht and Alexander, such a loading results in a variety of local loading paths in the considered domain testing a wide set of responses. Secondly, in their study severe scaling issues prevented the simulations

using the dogleg method from completing [46]<sup>||</sup>. Although in that case the GTN constitutive model was used, consideration of this problem tests the ability of the extra scaling terms to address this issue and provides a challenge for the proposed implementation.

The rod in question is taken to be 100 mm long ( $L = 100$  mm) with a circular cross section of radius 20 mm. All degrees of freedom along the top edge ( $x_3 = L$ ) are fixed ( $u_1 = u_2 = u_3 = 0$ ) while the bottom ( $x_3 = 0$ ) is constrained to remain planar ( $u_3 = 0$ ). To load the rod, a horizontal displacement of  $u_1^{app} = 50$  mm is applied along the bottom,  $x_3 = 0$ , face. Schematically, these conditions are presented in Fig. 5a. Two additional points (pt.  $A = (-r/2, 0, 0)$  and pt.  $B = (r/2, 0, 0)$ ) are indicated for subsequent analysis with the origin being at the center of the bottom face. For these simulations a fixed number of loading increments (200) is used and no global timestep cutbacks are allowed to better enable direct comparisons between the various results.

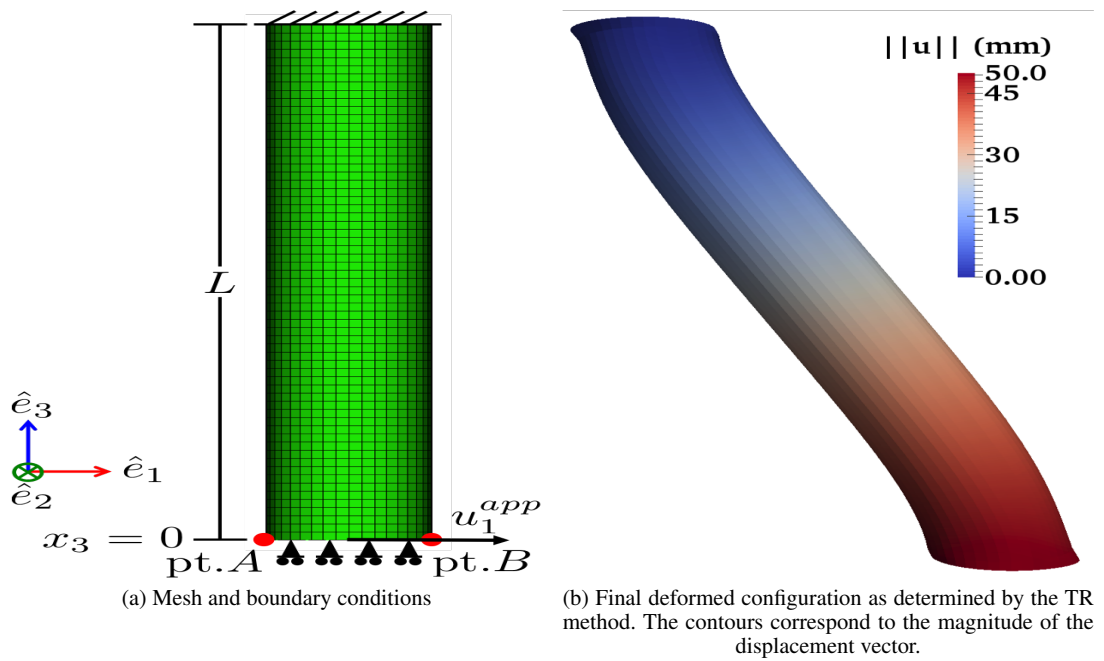


Figure 5. Summary of rod under combined tension and shear loadings: (a) Boundary conditions and mesh and (b) Final result

Results of the analyses are given in Figs. 5b and 6 and good agreement is noted between the various numerical implementations. Specifically, Fig. 5b shows the final, deformed configuration at the end of the loading as determined by the TR method highlighting the ability of the studied implementation to handle large deformations. An essentially identical result is also obtained for the LS-NR approach. Additionally, Fig. 6a presents the effective von Mises stress at pts.  $A$  and  $B$ , respectively, at different applied displacements. No measurable difference is found at either point between the LS-NR and TR methods at any applied loading further verifying the proposed implementations. Agreement is also observed with the NR method through about the first 60% of the simulation. At this point, the NR approach fails to converge. This comparison demonstrates the capability of the proposed algorithm to handle previously difficult BVPs.

To consider the relative performance and speed of the algorithms in these cases, the average (over the entire model) number of correction iterations needed at each point of the loading path is determined and plotted in Fig. 6b. In these cases, the average number of iterations is plotted

<sup>||</sup>In their study [46], the Levenberg-Marquardt approach was able to successfully analyze this problem. However, as the dogleg algorithm they discuss more closely resembles the current method, the performance of that approach is of more concern for motivation and comparison purposes.

in lieu of the maximum to better assess the overall performance of the algorithms rather than extremum cases. As can be seen in the results of Fig. 6b identical responses are noted for the LS-NR and TR implementations. Both of these approaches require fewer correction iterations than the more standard NR – highlighting additional benefits for these methodologies in terms of reducing computational cost.

As fixed time incrementation is used in these simulations, it is possible that the selected timestep sizes may influence performance of the various algorithms. To investigate this possibility, a second set of simulations utilizing only 100 loading increments are performed and the results presented in Fig. 6b. As expected, a slightly higher average number of correction iterations is required versus the 200 increment case. The same trends in comparing the three methods are also observed in this case highlighting the improved performance of the LS-NR and TR methods over the more traditional NR case. With respect to speed, no appropriate comparison is available between the NR and other methods due to lack of convergence in the former. In comparing the LS-NR and TR results, it is noted that the TR cases had 3.6% and 2.5% higher wallclock times than than the LS-NR approach for the 100 and 200 increment analyses, respectively. Although slightly more expensive, these timings again show comparable speed performance between the two implementations.

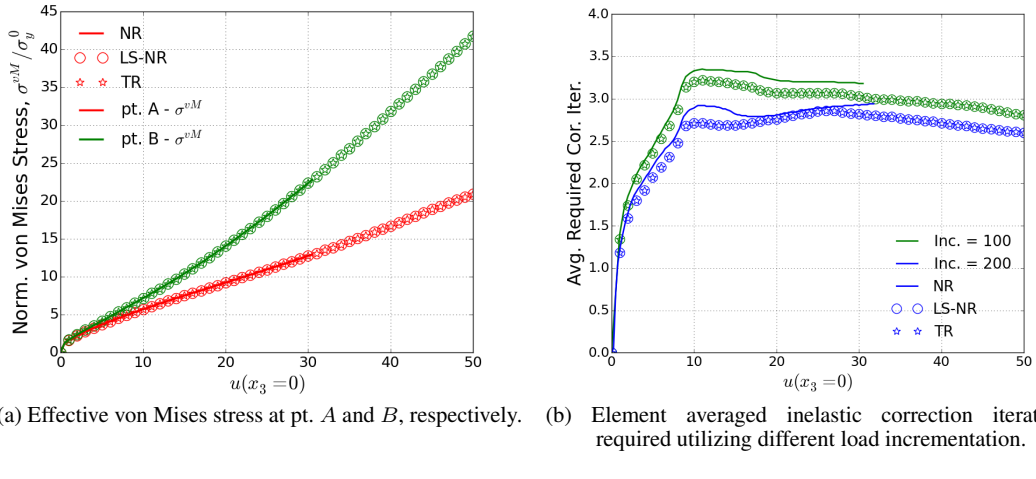


Figure 6. Results of rod tension/shear problem: (a) von Mises effective stress and (b) required correction iterations over loading as determined by the NR, LS-NR, and TR methods

### 3.2. Numerical Robustness

With the capabilities of the trust-region implementation verified through different boundary value problems, the next issue to consider is that of the robustness of the proposed algorithm. To that end, the methodology of Scherzinger [29] is adopted. Through this approach, a series of trial stress states are determined and used as input to the considered algorithm. The number of iterations needed to converge (or lack there of) is recorded. The considered initial stress states scan the  $\pi$ -plane between the initial yield surface and a surface whose equivalent effective stress is 30 times that of yield ( $\phi = 30\sigma_y^0$ ). Although quite large,  $30\sigma_y^0$  is selected as strain increments may be produced during inelastic deformation resulting in quite substantial trial stresses. Given that local convergence failure can lead to global time step cutbacks and potentially noticeable time costs, robustness under large trial stresses is desired. Additionally, in global FE implementations using a preconditioned conjugate gradient solver (like Sierra/SM [30, 32]) substantial variation in a displacement (strain) guess may be observed further necessitating robustness at seemingly excessive trial stress states. Sampling in this fashion results in over 95,000 trial stress states whose numerical response is considered.

First, three different yield exponents are considered ( $a = 6, 8$ , and  $100$ ) that sequentially increase the curvature of the yield surface. The former values are commonly used for BCC and FCC

metals, respectively [54], while the latter  $a = 100$  case approximates the Tresca yield surface and its numerically problematic corners. Trivial cases of  $a = 2$  and  $4$  corresponding to a von Mises yield surface are neglected as the results show a uniform, single step return mapping procedure as is expected for a radial-return. For these studies, perfect plasticity ( $K = 0$ ) is considered as Scherzinger [29] indicated hardening had little impact on algorithmic performance. For the TR algorithm, one correction must be made for usage in this analysis. Specifically, as no strain increment or previous material state is given a modification is needed for  $\bar{\Delta}$  in Eqn. 28. Therefore, following the motivations discussed regarding Eqn. 28, it is noted (i) the trial stress, not total strain increment, is used as input to the constitutive model (ii) with  $K = 0$  the effective stress measure of the solution stress will be equal to the yield value and (iii) the total strain increment corresponds to the elastic strain of the trial stress state. Therefore, for this study, the modified maximum trust-region radius is written as,

$$\bar{\Delta} = b^\sigma \sqrt{(\phi(\sigma_{ij}^{tr}) - \sigma_y^0)(\phi(\sigma_{ij}^{tr}) - \sigma_y^0)} + b^\gamma \sqrt{\frac{2}{3} \mathbb{C}_{ijkl}^{-1} \sigma_{kl}^{tr} \mathbb{C}_{ijmn}^{-1} \sigma_{mn}^{tr}}. \quad (37)$$

The convergence maps for the case of yield exponents  $a = 6, 8$ , and  $100$  are presented in Fig. 7. These maps present the number of correction iterations needed to achieve convergence at a given trial stress space with the results projected onto the deviatoric  $\pi$ -plane. Lighter colors denote fewer correction iterations and points marked in red do not converge by the 40<sup>th</sup> iteration.

Importantly, between the three convergence maps in Fig. 7 it is observed that the TR algorithm converges for almost every case by the 40<sup>th</sup> iteration. In fact, all considered trial stresses for the  $a = 6$  and  $8$  cases do converge by the specified iteration. A few ( $< 1\%$ ), isolated points may be found in the  $a = 100$  Tresca-like case that do not converge by the 40<sup>th</sup> iteration. Furthermore, as expected the three maps exhibit a six-fold symmetry that is anticipated for the isotropic yield surface. Additionally, it can clearly be seen that as the exponent and corresponding curvature increases so do the number of required iterations. The  $a = 6$  cases shows a fairly uniform light coloration indicating relatively easy convergence for most cases – even at substantial trial stresses. At the higher  $a = 8$  value, some more computational difficulty arises in domains closer to the higher curvature areas. In the limit case of  $a = 100$  a generally more expensive convergence may be observed. A more diffuse map is noted but a clear trend of increased correction iterations nearest the corners is evident. Additionally, the cases that do not converge by the 40<sup>th</sup> seem to occur at the edges of these domains.

To more extensively compare the results presented in Fig. 7, cumulative distributions of the total percentage of sampled cases that have successfully converged by a given correction iteration are presented in Fig. 8. Although the convergence maps for the NR and LS-NR cases are not presented in this work (see Scherzinger [29]), their responses were calculated and the corresponding cumulative convergence distributions are also presented in Fig. 8. It should be noted that given the sampling used to generate Fig. 7, the current distributions do not correspond to that expected during a typical boundary value problem.

From the results of Fig. 8, a number of important observations regarding the convergence characteristics of the three methods may be discerned. First, in all three cases, the response of the different methods through the first four correction iterations is quite similar. At this point, the converged cases of the LS-NR approach increase at a quicker rate than the other two cases. Eventually, for all three exponents, the TR implementation has a higher percentage of converged trial stresses the LS-NR. As the exponent increases the percentage of converged case at which the TR algorithm has a higher cumulative convergence decreases. At this stage, the number of cases converging per iteration decreases and both the LS-NR and TR method approach complete convergence (100% cumulative convergence). The NR implementation, however, cannot achieve complete convergence and fewer cases converge with larger exponents. Importantly, for all of the considered yield surfaces the LS-NR and TR method *always* converge. In the  $a = 100$  case this does not always occur by the 40<sup>th</sup> iteration, but it does occur within 60. These problematic trial stresses represent much less than 1% of the tested cases. To summarize the capabilities of the different numerical schemes, the number of iterations needed to achieve complete, 100% cumulative convergence are given in Table II. As would be expected, increase in the curvature of the yield

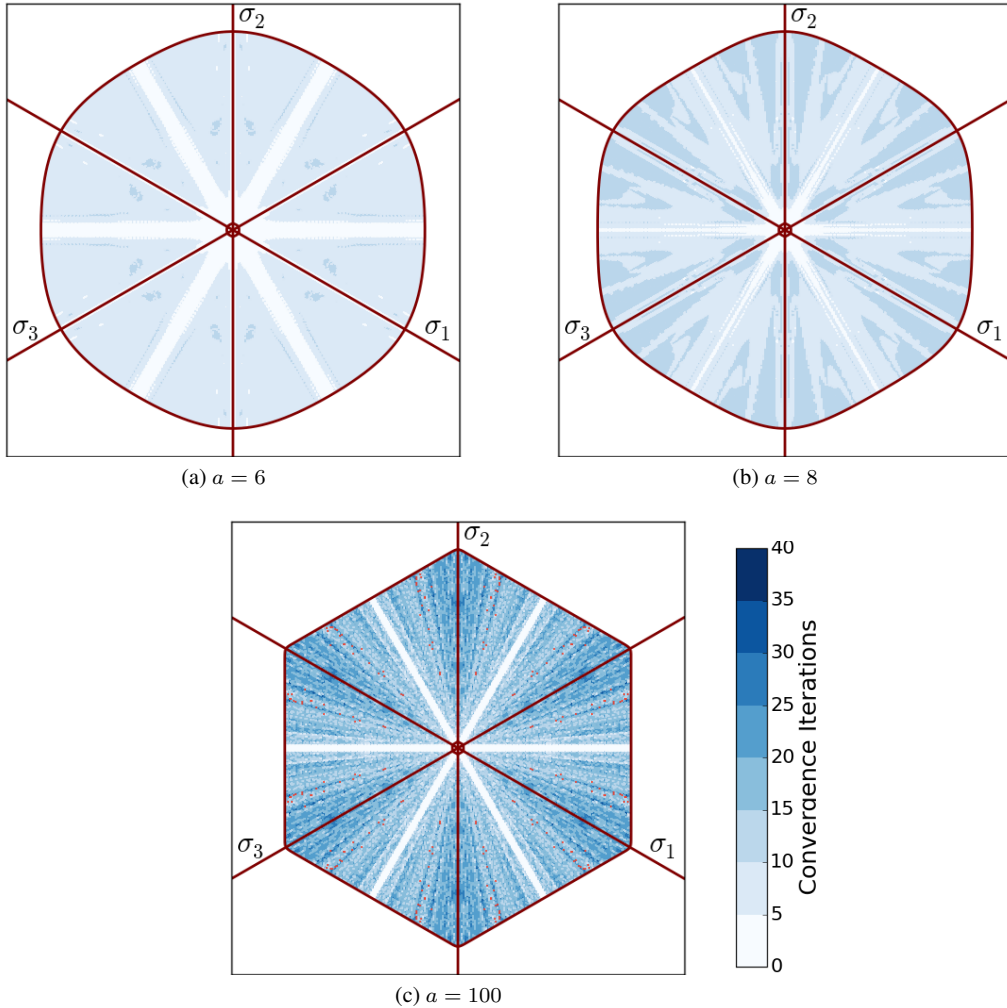


Figure 7. Convergence maps for the TR algorithm giving the number of correction iterations needed at a trial stress state in deviatoric space to achieve convergence. Three Hosford yield surface with different exponents,  $a$ , are considered. The same scale is used for all figures and points that do not converge within 40 iterations are marked red.

surface (reflected in higher values of  $a$ ) leads to more iterations required to achieve complete convergence.

$a$	NR	LS-NR	TR
6	-	11	12
8	-	24	16
100	-	45	52

Table II. Number of iterations required to achieve complete, 100% cumulative convergence for different Hosford yield exponents ( $a$ ) for the NR, LS-NR, and TR approaches.

Based on these results, the TR performance is clearly superior to the NR method in terms of robustness. With respect to the LS-NR method, such a distinction is less clear. Figure 9 explores such a comparison by presenting the iteration difference between the two approaches. Specifically, in Fig. 9a a  $\pi$ -plane map in which the iteration change in going to the TR approach from that of the LS-NR is plotted for the  $a = 8$  case. Put another way, the iteration change is equal to the iterations

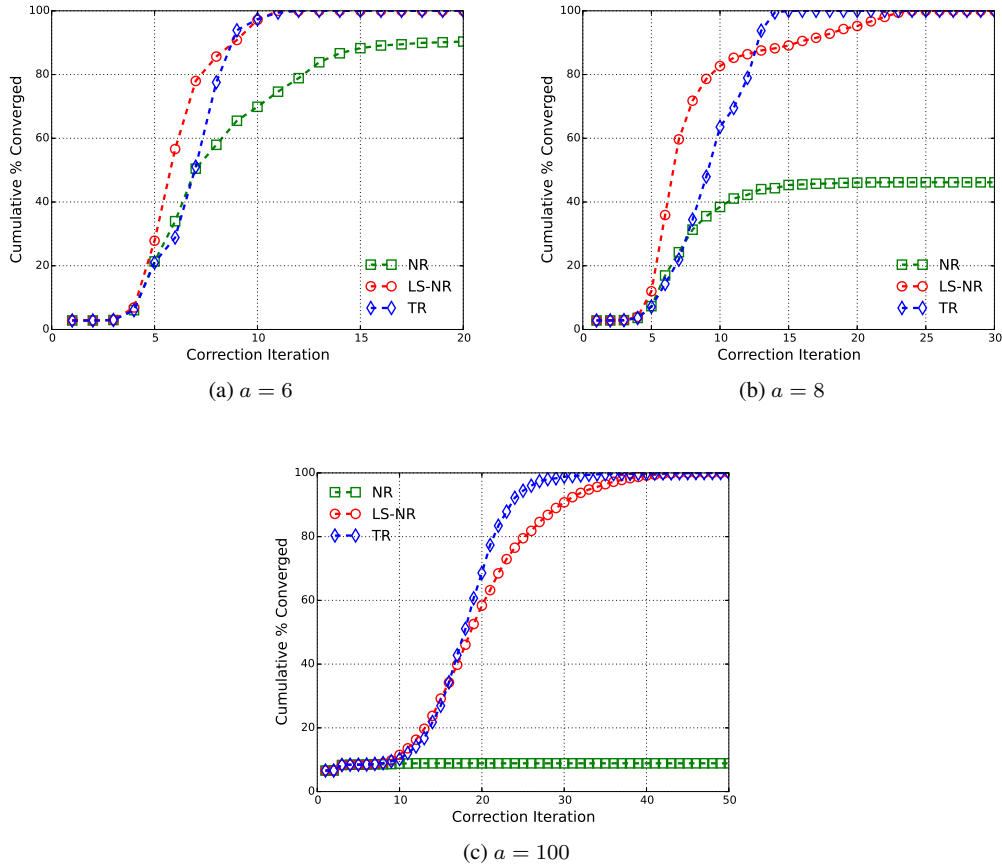


Figure 8. Cumulative convergence distributions of NR, LS-NR, and TR methods for three different Hosford yield surface exponents,  $a$ . Considered cases come from sampling the  $\pi$ -plane at locations whose scalar effective stresses are  $\sigma_y < \phi(\sigma_{ij}^{tr}) \leq 30\sigma_y$ .

needed for the TR method minus those of the LS-NR approach. As such, trial stress states in red indicate regions in which the TR algorithm requires more correction iterations than the LS-NR and blue indicates areas in which the TR approach requires fewer correction iterations and therefore exhibits superior performance. Regions in green denote cases in which the TR required at least ten fewer correction iterations. In terms of extremes, the proposed TR scheme required eighteen fewer or ten addition correction iterations versus the LS-NR. From the results of Fig. 9, it may be observed that the two algorithms show nearly identical convergence behaviors in domains with smaller effective stress measures. At trial stresses with larger effective stresses, substantial gains (in terms of needed iterations) may be obtained by using the TR method in some shear dominated domains. Figure 9b expands on this by presenting the average change in correction iterations for a given effective stress measure for all three yield exponents. Averaging in this fashion sample considers a variety of stress states (e.g. shear-dominated; uniaxial) and yields a representative metric for a given stress level. From such an analysis, it is observed that at lower stress measures there is no difference in required number of iterations. As the yield exponent  $a$  increases, however, the length of this similarity decreases. For the smallest exponent considered, the LS-NR algorithm outperforms (in terms of correction iterations) the TR at all effective stress levels. At the larger  $a = 8$  value, regions in which both TR and LS-NR algorithm exhibit superior performances are clearly observed. When the curvature approaches that of Tresca ( $a = 100$ ), large oscillations are seen in the iteration differences. None the less, the trend of the response is that TR seems to perform better than the

LS-NR at most effective stress levels. These results indicate the TR algorithm may hold promise for more computationally challenging problems.

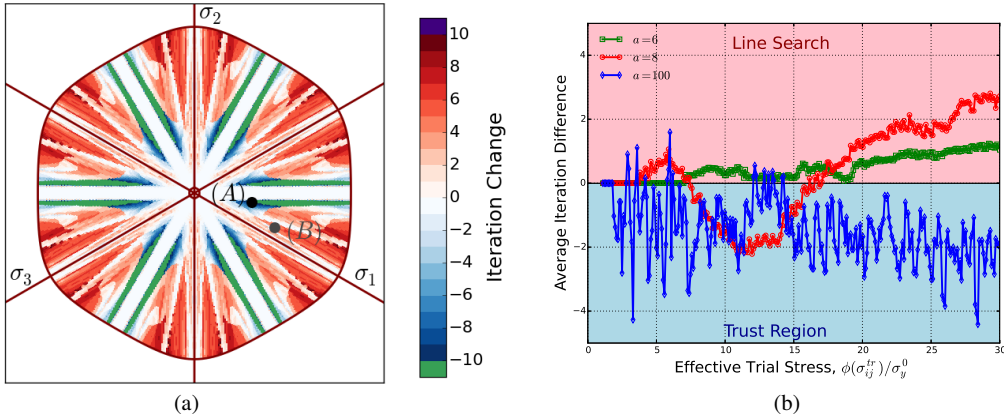


Figure 9. Iteration change ( $\text{iter}(\text{TR}) - \text{iter}(\text{LS-NR})$ ) needed by the TR algorithm versus the LS-NR approach: (a)  $\pi$ -plane map in which any trial stress state requiring 10 or more fewer iterations is colored green while any case needing 10 or more additional iterations is shaded purple; (b) average number of correction iterations needed for a given effective stress measure. The results correspond to the  $a = 8$  Hosford yield surface and two specific stress states in (a) are labelled (A) and (B) for later analysis.

To consider the convergence characteristics and response of the TR algorithm more closely, two trial stresses are marked in Fig. 9a. The first, marked (A), corresponds to a trial stress state,  $\sigma_{ij}^{tr(A)}$ , with principal components  $\sigma_1 = 1,378$  MPa,  $\sigma_2 = -242$  MPa, and  $\sigma_3 = -1,135$  MPa and is one of lower effective trial stress states showing a more than 10 iteration improvement in going to the TR method. The second, marked (B), is for a trial stress state,  $\sigma_{ij}^{tr(B)}$  whose principal components are  $\sigma_1 = 2,187$  MPa,  $\sigma_2 = -876$  MPa, and  $\sigma_3 = -1,311$  MPa and is selected for the opposite reason. In this case, the TR implementation required six more iterations. Figures 10 and 12 explore the source of these differences by presenting the return mapping (convergence) trajectories. These trajectories start from the trial stress state (denoted as the “0” iteration) and plot the successive states that are found during the return mapping process. In this way, the path taken during the inelastic correction process may be visualized to compare and analyze the performance of the different algorithms.

In Fig. 10, the return mapping processes of the NR (10a), LS-NR (10b), and TR (10c) algorithms with a trial stress of  $\sigma_{ij}^{tr(A)}$  are presented. Figure 11 gives the evolution of the merit function for the LS-NR and TR approaches along with the scaled trust-region radius during inelastic correction. From the results of these two figures, it is observed that the return path of the TR implementation differs from the other two in the very first iteration. Specifically, the NR and LS-NR both take a substantial step that brings the stress state much closer to the yield surface but overshoots in terms of flow direction. This leads to a second step that attempts to correct the direction but again goes too far. The LS-NR algorithm is eventually able to find the correct direction and descend to the yield surface using a large number of step size cutbacks (see Scherzinger [29]). In Fig. 11, this manifests as the set of iterations with only small changes to the merit function. As the NR approach cannot cutback, it is unable to compensate and cannot converge. The TR approach, on the other-hand, actually rejects this initial step and cuts back on the scaled TR radius as shown in Fig. 11. This leads to a much smaller second correction iteration for the TR that does not overshoot the desired flow direction. Subsequent steps then eventually find the correction direction and converge to the solution in far fewer iterations than the LS-NR approach.

Figures 12 and 13 present the return mapping processes of the the algorithms and merit function and scaled trust-region evolution, respectively, for the opposite case ( $\sigma_{ij}^{tr(B)}$ ) in which the LS-NR (and NR) approaches outperform the TR. Initially, the return paths of the three methods are similar to that discussed for Fig. 10. The LS-NR and NR both take large initial steps while the

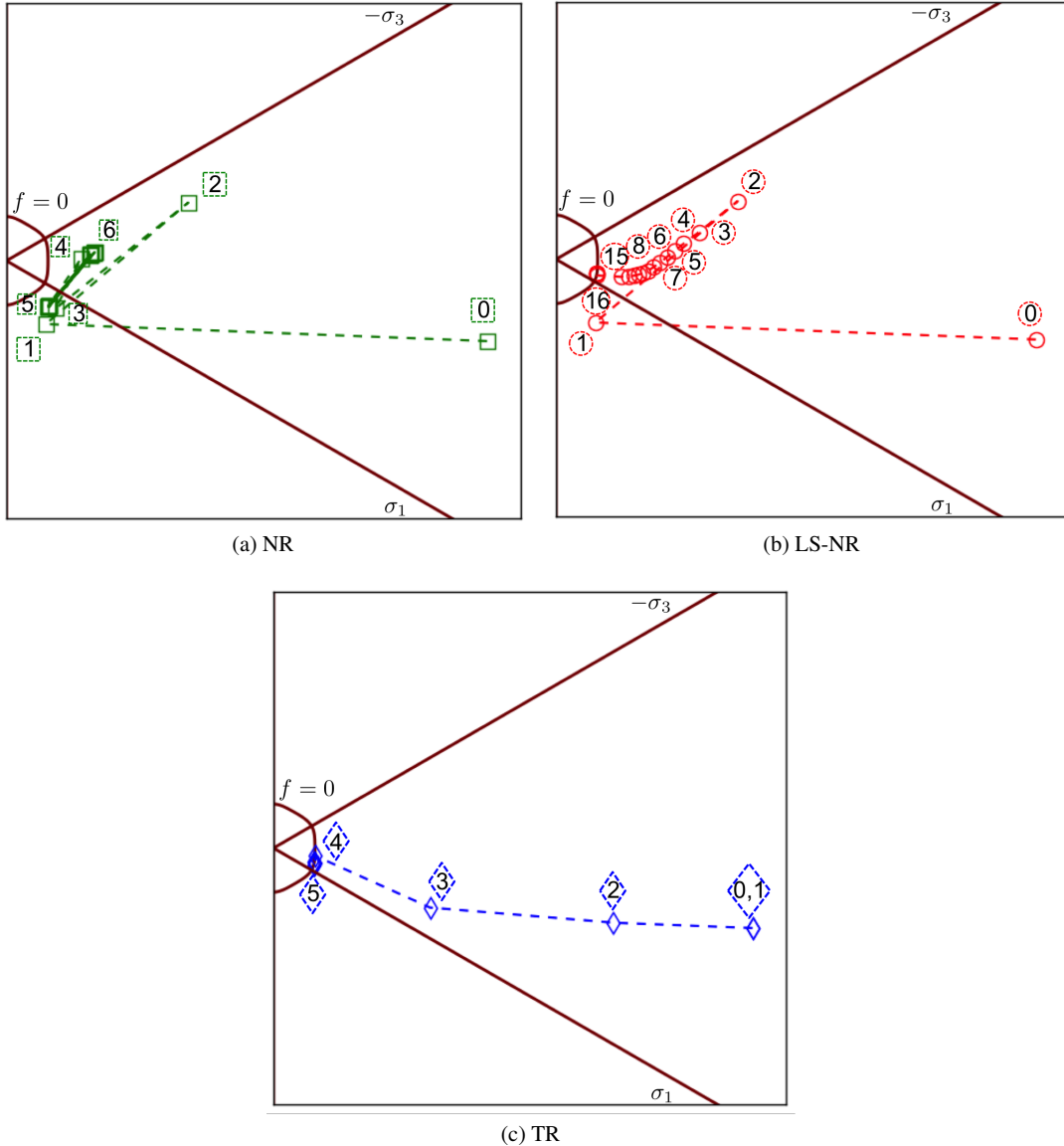


Figure 10. Inelastic correction process of the CPP-RMA problem solved by the (a) NR, (b) LS-NR, and (c) TR algorithms with an initial trial stress of  $\sigma_{ij}^{tr(A)}$ . The marked points are used to indicate the current correction iteration for select points. As the NR algorithm does not converge, only the first 20 iterations are plotted.

TR implementation rejects the first, large step. Unlike the previous results, the second correction for the LS-NR and NR algorithms finds the correct direction and quickly descend to the solution. Similar to the previous case, the TR approach seeks to find the correct direction early and descend to the correct solution. As indicated in Figs. 12c and 13, however, this requires multiple iterations being rejected and TR radius cutbacks. This leads to more correction steps than the LS-NR and NR approaches. Interestingly, the fact that in both these cases the TR seeks to stay so close to the correct descent direction is likely indicative of the scaling introduced into the merit function.

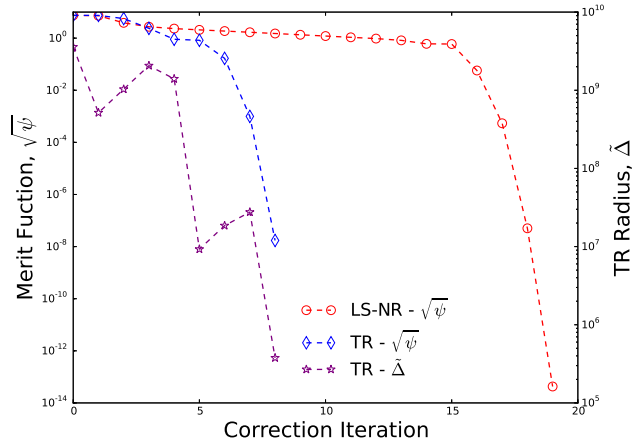


Figure 11. Merit function,  $\psi$ , and TR radius,  $\tilde{\Delta}$  evolution through the LS-NR and TR inelastic correction process associated with an initial trial stress of  $\sigma_{ij}^{tr(A)}$ .

### 3.3. Impact of Scaling

Trust-region methods and the performance of corresponding algorithms are known to be sensitive to scaling. Previously, two transformations were introduced –  $D_{IJ}^1$  in Eqn. 13 and  $D_{IJ}^2$  in Eqn. 22 – to address scaling in the merit function and state variable increments, respectively. Up to this point, these values have been fixed with limited motivation as to their selection. The impact of these terms on the performance of TR algorithm has also not been determined or addressed. These issues are investigated in this section. First, to consider the impact of the relative contrast of merit function components, a modified weighting constant for the flow rule residual of the form  $c^\varepsilon = \beta (E/\sigma_y^0)$  is introduced with  $\beta$  being a constant. At this point, it is emphasized that  $\beta$  is neither a material model nor algorithmic parameter. It is instead an artificial scaling variable introduced to study the effect of the relative scaling of the two residual contributions. To determine the range of  $\beta$ , it is noted that  $c^\varepsilon$  and  $c^f$  differ by  $E$  whose magnitude is  $2.0 \times 10^{11}$ . Therefore, to consider the maximum contrast between a scaled merit function and one utilizing both stress and strain terms, the range  $10^{-11} \leq \beta \leq 10^0$  will be explored. As such, the larger values of  $\beta$  correspond more closely to the properly scaled cases studied throughout earlier sections of this work. Smaller artificial scalings lead to more substantial deviations from what has been used and essentially serve to decrease the contribution of the flow rule residual,  $r_{ij}^\varepsilon$ , in the merit function evaluation.

Figure 14 presents a summary of cumulative convergence distributions (like those in Fig. 8) determined for 200 different values of  $\beta$ . Specifically, for each artificial scaling the necessary number of iterations needed to first achieve *at least* cumulative convergences of 10%, 25%, 50%, 75%, and 100% are presented. If the specified threshold is not reached for a given value of  $\beta$ , it is not plotted. The percentage of unconverged states (after 100 iterations) is also presented to highlight any lack of convergence. As iterations occur only in discrete values, the actual cumulative convergence at these points will not match the given limit value exactly. From the results in Fig. 14, it can be observed that scaling and the relative contrast between the residual terms in the merit function play a strong role in the performance of the TR algorithm. For instance, only properly scaled cases ( $\beta \approx 10^{-2}$ ) exhibit complete convergence while artificially scaled problems ( $\beta \leq 10^{-3}$ ) converge for less than 30% of the trial stress states and may be considered poorly scaled. As such, it can clearly be seen that careful selection of normalization constants is necessary for the TR implementation.

To investigate the source of the strong scaling dependence of the proposed approach, Fig. 15 presents the return mapping process of a case with no artificial scaling,  $\beta = 10^0$ , and one with moderate artificial scaling ( $\beta = 10^{-3}$ ). The trial stress state in this study corresponds to  $\sigma_{ij}^{tr(A)}$ .

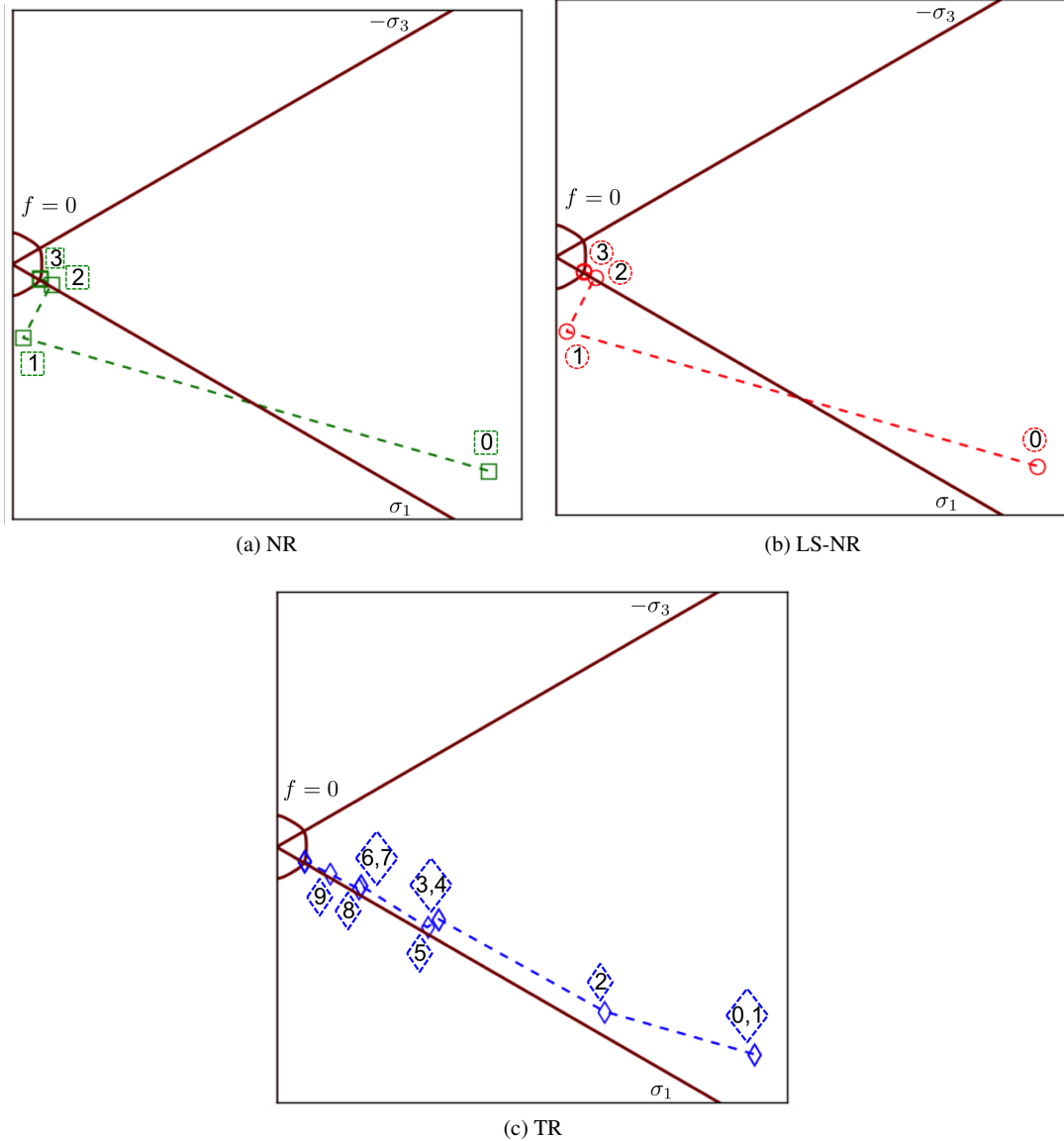


Figure 12. Inelastic correction process of the CPP-RMA problem solved by the (a) NR, (b) LS-NR, and (c) TR algorithms with an initial trial stress of  $\sigma_{ij}^{tr(B)}$  (MPa). The marked points indicate the current correction iteration although for clarity not all points are labelled.

presented in Fig. 10. For the artificially scaled response, the first 100 iterations are presented while the  $\beta = 10^0$  response corresponds to the TR results previously presented and discussed in Fig. 10c. In Fig. 15a, it can be observed that the the inappropriately scaled case ( $\beta = 10^{-3}$ ) initially takes the large step bypassed by the correctly scaled case. This indicates the impact of the scaling on the algorithm performance as this large step is now acceptable in terms of improvement in the merit function. Subsequent iterations head straight to the yield surface albeit well away from the appropriate location. Given the poor scaling of the problem, the successive correction steps are unable to move away and instead oscillate around the surface ever so slowly heading towards the correct solution (Fig. 15b). In this context, the decreased  $\beta$  leads to the consistency condition contribution dominating the model problem underlying the TR approach. Therefore, unless the merit

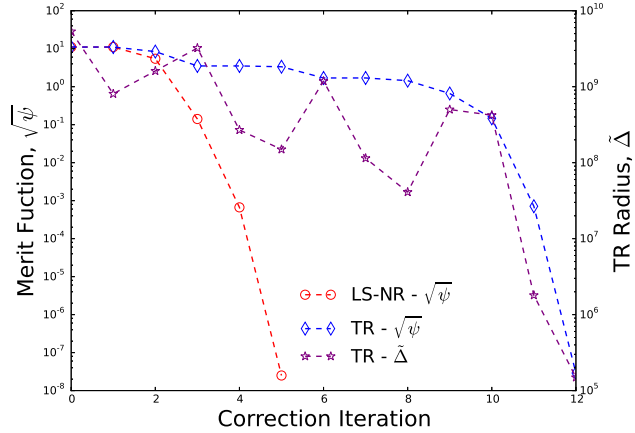


Figure 13. Merit function,  $\psi$ , and TR radius,  $\tilde{\Delta}$  through the LS-NR and TR inelastic correction process associated with an initial trial stress of  $\sigma_{ij}^{tr(B)}$ .

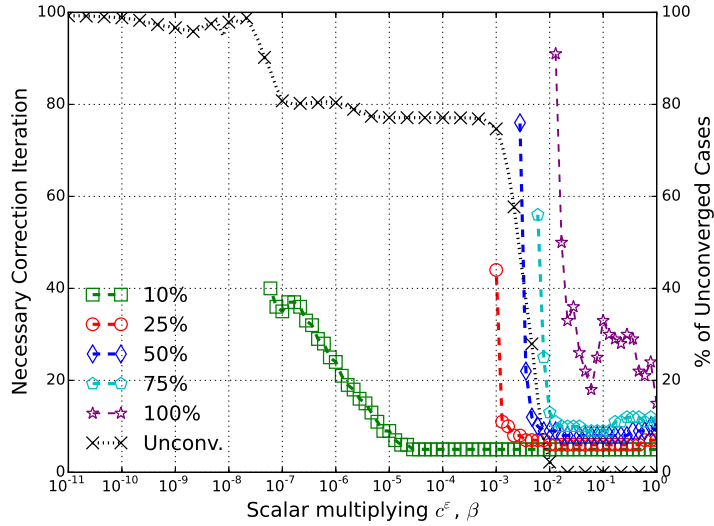


Figure 14. Influence of relative contrast between  $c^e$  and  $c^f$  on the convergence characteristics of the proposed TR method. Results correspond to the necessary number of correction iterations to achieve the specified cumulative convergence threshold as a function of the artificial scaling parameter,  $\beta$ , in which  $c^e = \beta (E/\sigma_y^0)$ .

function is properly scaled, the TR method cannot simultaneously satisfy the two conditions at the heart of the inelastic correction problem.

The second potential source of scaling is associated with the state variables and is addressed via selection of  $b^\sigma$  and  $b^\gamma$ . In all previous cases,  $b^\sigma = 1$  and  $b^\gamma = 2\mu$  which given the selected material properties corresponds to a difference of roughly eleven orders of magnitude. To investigate this effect, the cumulative convergence thresholds utilizing a plastic consistency scaling of  $b^\gamma = \beta 2\mu$  (with  $10^{-11} \leq \beta \leq 10^0$ ) are determined as a function of the artificial scaling parameter,  $\beta$ , and the corresponding results are plotted in Fig. 16. In Fig. 16a,  $b^\gamma$  is scaled independently of the merit function to isolate the impact of the state variable terms.

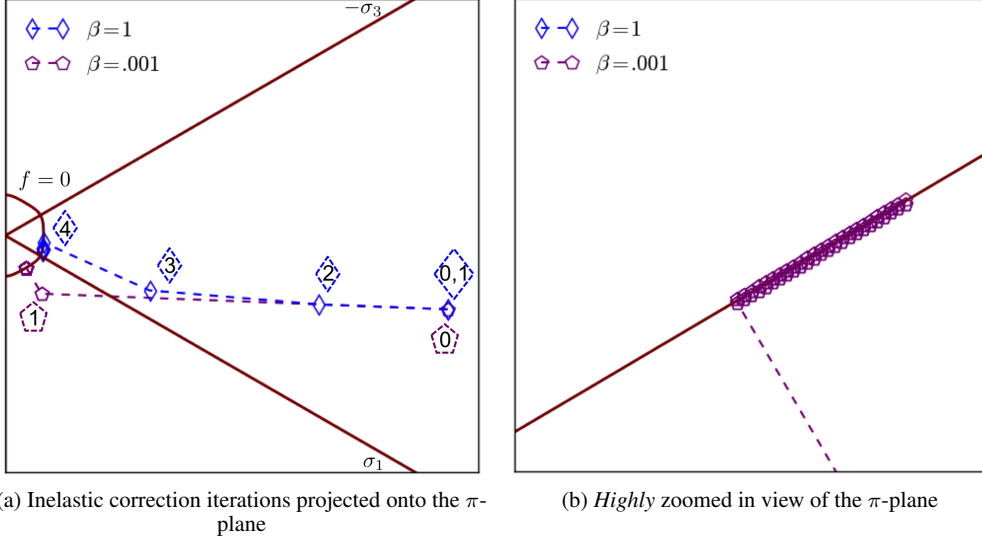


Figure 15. Inelastic correction process of trust-region (TR) method using two different stress normalization scalings for the  $a = 8$  yield surface with an initial trial stress of  $\sigma_{ij}^{tr} = \sigma_{ij}^{tr(A)}$  (MPa). The results are presented in terms of the artificial scaling parameters,  $\beta$ , where  $c^\varepsilon = \beta (E/\sigma_y)$ .

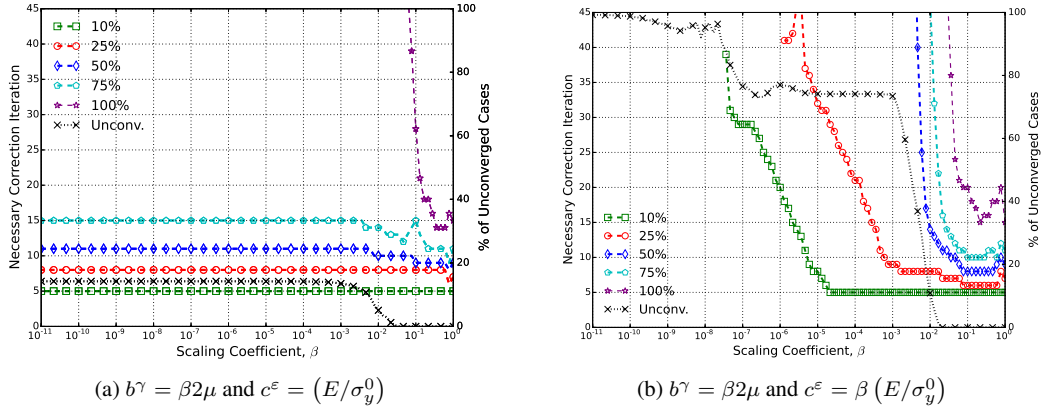


Figure 16. Influence of scaling the state variables on the convergence characteristics of the trust-region method in terms of the artificial scaling parameter,  $\beta$ .

From the results of Fig. 16a, a moderate dependence on the scaling of  $b^\gamma$  is observed. Specifically, complete convergence is only achieved with scalings such that the consistency multiplier is still roughly stress measured ( $b^\gamma > \approx 0.2\mu$ ). However, when poorly scaled ( $\beta \leq 10^{-3}$ ) the necessary correction iterations to achieve the remaining convergence thresholds do not change and only increase by one or two iterations versus their lowest values. Additionally, convergence is achieved for more than 80% of the considered trial stress states regardless of the artificial scaling coefficient. This response is in contrast to the impact of the merit function scaling (Fig. 14) in which a pronounced effect is observed with  $\beta$  and very few cases are able to converge. Therefore, it is reasonable to state that although appropriate scaling of the state variable coefficients is necessary to achieve the desired robustness, the dependence is far less severe than on the merit function constants.

Given the disparity between the scaling dependence of the merit function and state variables, one possibility to try and alleviate the convergence difficulties of the former is to scale both terms together. This course is investigated in Fig. 16b and the corresponding results are observed to much more closely follow the merit function scaling trends than those of  $b^\gamma$ . Specifically, complete convergence is only achieved when properly scaled ( $\beta > \approx 10^{-2}$ ) and limited convergence is seen over the rest of the domain. Although similar to the results of Fig. 14 some differences may be observed. Specifically, the 25% convergence threshold is achieved over a larger  $\beta$  range and some limits (*e.g.* 100%) require fewer iterations. With respect to this latter point, no clear trend is observed. In any case, these results serve as further evidence that inappropriate scaling in the merit function leads to drastically reduced performance of the TR method. Additionally, scaling the state variables in a similar fashion cannot rectify this issue.

#### 4. CONCLUDING REMARKS

In this work, a novel method utilizing the TR method for the implicit integration of plasticity models is presented. Unlike previous approaches, the non-linear equations forming the core of stress updating procedure are not solved via the Newton-Raphson method thereby bypassing the corresponding robustness issues and avoiding the use of substepping or line search techniques. The proposed methodology was discussed in detail and implemented for a Hosford plasticity model. Through a series of boundary value problems, the model response was verified against traditional NR and LS-NR schemes with only a slight increase in computational cost. Importantly, by using an algorithm tailored for constitutive model integration, the current implementation was able to solve the problem of a rod loaded in tension and shear that could not be solved with just a NR implementation and vexed a previous dogleg TR approach. The robustness of the proposed algorithm was studied in detail and demonstrated to exhibit convergence characteristics similar to that of the LS-NR method and far in excess of the NR performance *when properly scaled*. It was also clearly shown that the scaling issues in the TR approach are substantial and the merit function and state variable vector must be scaled to achieve the desired algorithmic performance. Of the two, the merit function was shown to be more potent and the performance of the proposed implementation quickly deteriorates without appropriate treatment.

Given the performance reported through this effort, the proposed routine detailed here represents an exciting possibility towards improved constitutive integration schemes. To this end, the current implementation is a first attempt at using TR methods that have been developed in the optimization community for other purposes. Potential improvements via specialized model problem formulation or alternatives to the dogleg method could increase efficiency and drive down cost. Additionally, the possibilities of this approach to further improve on the performance for more challenging models with anisotropy, alternative and/or coupled physics (*i.e.* damage or tight thermomechanical coupling), and multisurface cases is enticing. Such investigations shall be pursued in future efforts.

#### ACKNOWLEDGEMENTS

The original inspiration and suggestion for this work arose out of comments and discussions from Jakob Ostien, James W. Foulk III, and Alejandro Mota of Sandia National Laboratories. Their comments in this regard are greatly appreciated. Sandia National Laboratories is a multi-program laboratory managed and operated by Sandia Corporation, a wholly owned subsidiary of Lockheed Martin Corporation, for the U.S. Department of Energy's National Nuclear Security Administration under contract DE-AC04-94AL85000.

#### REFERENCES

1. Hosford WF. A generalized isotropic yield criterion. *Journal of Applied Mechanics* 1972; **39**:607–609.

2. Hill R. *The Mathematical Theory of Plasticity*. Clarendon Press: Oxford, 1950.
3. Barlat F, Aretz H, Yoon JW, Karabin ME, Brem JC, Dick RE. Linear transformation-based anisotropic yield functions. *International Journal of Plasticity* 2005; **21**:1009–1039.
4. Barlat F, Yoon JW, Cazacu O. On linear transformations of stress tensors for the description of plastic anisotropy. *International Journal of Plasticity* 2007; **23**:876–896.
5. Karafillis A, Boyce MC. A general anisotropic yield criterion using bounds and a transformation weighting tensor. *Journal of Mechanics and Physics in Solids* 1993; **41**(12):1859–1886.
6. Cazacu O, Barlat F. A criterion for description of anisotropy and yield differential effects in pressure-insensitive metals. *International Journal of Plasticity* 2004; **20**:2027–2045.
7. Cazacu O, Plunkett B, Barlat F. Orthotropic yield criterion for hexagonal closed packed metals. *International Journal of Plasticity* 2006; **22**:1171–1194.
8. Yoon JW, Barlat F, Dick RE, Chung K, Kang TJ. Plane stress yield function for aluminum alloy sheets – part II: FE formulation and its implementation. *International Journal of Plasticity* 2004; **20**:495–522.
9. Yoon JW, Barlat F, Dick RE, Karabin ME. Prediction of six or eight ears in a drawn cup based on a new anisotropic yield function. *International Journal of Plasticity* 2006; **22**:174–193.
10. Safaei M, Lee MG, De Waele W. Evaluation of stress integration algorithms for elastic-plastic constitutive models based on associated and non-associated flow rules. *Computer Methods in Applied Mechanics and Engineering* 2015; **295**:414–445.
11. Korkolis YP, Kyriakides S. Inflation and burst of aluminum tubes. Part II: An advanced yield function including deformation-induced anisotropy. *International Journal of Plasticity* 2008; **24**:1625–1637.
12. Korkolis YP, Kyriakides S. Path-dependent failure of inflated aluminum tubes. *International Journal of Plasticity* 2009; **25**:2059–2080.
13. Korkolis YP, Kyriakides S, Giagmouris T, Lee LH. Constitutive modeling and rupture predictions of Al-6061-T6 tubes under biaxial loading paths. *Journal of Applied Mechanics* 2010; **77**:064 501.
14. Ortiz M, Pinsky PM, Taylor RL. Operator split methods for the numerical solution of the elastoplastic dynamic problem. *Computer Methods in Applied Mechanics and Engineering* 1983; **39**:137–157.
15. Simo JC, Ortiz M. A unified approach to finite deformation elastoplastic analysis based on the use of hyperelastic constitutive equations. *Computer Methods in Applied Mechanics and Engineering* 1985; **49**:221–245.
16. Ortiz M, Popov EP. Accuracy and stability of integration algorithms for elastoplastic constitutive relations. *International Journal for Numerical Methods in Engineering* 1985; **21**:1561–1576.
17. Simo JC, Taylor RL. A return mapping algorithm for plane stress elastoplasticity. *International Journal for Numerical Methods in Engineering* 1986; **22**:649–670.
18. Ortiz M, Simo JC. An analysis of a new class of integration algorithms for elastoplastic constitutive relations. *International Journal for Numerical Methods in Engineering* 1986; **23**:353–365.
19. Simo J, Hughes T. *Computational Inelasticity, Interdisciplinary Applied Mathematics*, vol. 7. Springer-Verlag: New York, NY, 1998.
20. Beteagón C, del Coz JJ, Penuelas I. Implicit integration procedure for viscoplastic Gurson materials. *Computer Methods in Applied Mechanics and Engineering* 2006; **195**:6146–6157.
21. Keavey MA. A simplified canonical form algorithm with application to porous metal plasticity. *International Journal for Numerical Methods in Engineering* 2006; **65**:679–700.
22. Nodargi NA, Bisegna P. State update algorithm for isotropic elastoplasticity by incremental energy minimization. *International Journal for Numerical Methods in Engineering* 2015; doi:10.1002/nme.4966.
23. Voyatzis GZ, Abed FH. Implicit algorithm for finite deformation hypoelastic-viscoplasticity in fcc metals. *International Journal for Numerical Methods in Engineering* 2006; **67**:933–959.
24. Qidwai MA, Lagoudas DC. Numerical implementation of a shape memory alloy thermomechanical constitutive model using return mapping algorithms. *International Journal for Numerical Methods in Engineering* 2000; **47**:1123–1168.
25. Semenov AS, Liskowsky AC, Balke H. Return mapping algorithms and consistent tangent operators in ferroelectroelasticity. *International Journal for Numerical Methods in Engineering* 2010; **73**:1298–1340.
26. Yoon JW, Yang DY, Chung K, Barlat F. A general elasto-plastic finite element formulation based on incremental deformation theory for planar anisotropy and its application to sheet metal forming. *International Journal of Plasticity* 1999; **15**:35–67.
27. Yoon JW, Yang DY, Chung K. Elasto-plastic finite element method based on incremental deformation theory and continuum based shell elements for planar anisotropic sheet materials. *Computer Methods in Applied Mechanics and Engineering* 1999; **174**:23–56.
28. Pérez-Foguet A, Armero F. On the formulation of closest-point projection algorithms in elastoplasticity – part II: Globally convergent schemes. *International Journal for Numerical Methods in Engineering* 2002; **53**:331–374.
29. Scherzinger WM. Return mapping algorithm for plasticity models using a line search method. *Computer Methods in Applied Mechanics and Engineering* 2016; Submitted.
30. Mitchell JA, Gullerud AS, Scherzinger WM, Koteras R, Porter VL. Adagio: non-linear quasi-static structural response using the SIERRA framework. *Proceedings of the First MIT Conference on Computational Fluid and Solid Mechanics*, Elsevier, 2001; 1–4.
31. Sierra/SM Development Team. Sierra/SM 4.40 verification tests manual. *SAND Report 2016-3083*, Sandia National Laboratories, Albuquerque, NM and Livermore, CA 2016.
32. Sierra/SM Development Team. Sierra/SM 4.40 user's guide. *SAND Report 2016-2707*, Sandia National Laboratories, Albuquerque, NM and Livermore, CA 2016.
33. Seifert T, Schenk T, Schmidt I. Efficient and modular algorithms in modeling finite inelastic deformations: Objective integration, parameter identification and sub-stepping techniques. *Computer Methods in Applied Mechanics and Engineering* 2007; **196**:2269–2283.
34. Seifert T, Maier G. Consistent linearization and finite element implementation of an incrementally objective canonical form return mapping algorithm for large deformation inelasticity. *International Journal for Numerical*

*Methods in Engineering* 2008; **75**:690–708.

35. Rabahallah M, Balan T, Bouvier S, Teodosiu C. Time integration scheme for elastoplastic models based on anisotropic strain-rate potentials. *International Journal for Numerical Methods in Engineering* 2009; **80**:381–402.
36. Dutko M, Perić D, Owen DRJ. Universal anisotropic yield criterion based on superquadric functional representation: Part 1. algorithmic issues and accuracy analysis. *Computer Methods in Applied Mechanics and Engineering* 1993; **109**:73–93.
37. Seifert T, Schmidt I. Line-search methods in general return mapping algorithms with application to porous plasticity. *International Journal for Numerical Methods in Engineering* 2008; **73**:1468–1495.
38. Nocedal J, Wright SJ. *Numerical Optimization*. 2 edn., Springer Series in Operations Research and Financial Engineering, Springer Science+Business Media: New York, NY, 2006.
39. Sorensen DC. Newton's method with a model trust region modification. *SIAM Journal of Numerical Analysis* 1982; **19**(2):409–426.
40. Powell MJD. On the global convergence of trust region algorithms for unconstrained minimization. *Mathematical Programming* 1984; **29**:297–303.
41. Gertz EM. A quasi-Newton trust-region method. *Mathematical Programming* 2004; **100**:447–470, doi: 10.1007/s10107-004-0511-1.
42. Ye F, Liu H, Zhou S, Liu S. A smoothing trust-region Newton-CG method for minimax problem. *Applied Mathematics and Computation* 2008; **199**:581–589.
43. Gratton S, Sartenaer A, Toint PL. Recursive trust-region methods for multiscale nonlinear optimization. *SIAM Journal of Optimization* 2008; **19**(1):414–444.
44. Sunar M, Belegundu AD. Trust region methods for structural optimization using exact second order sensitivity. *International Journal for Numerical Methods in Engineering* 1991; **32**:275–293.
45. Bergmann M, Cordier L. Optimal control of the cylinder wake in the laminar regime by trust-region methods and POD reduced-order models. *Journal of Computational Physics* 2008; **227**:7813–7840.
46. Shterenlikht A, Alexander NA. Levenberg-Marquardt vs Powell's dogleg method for Gurson-Tvergaard-Needleman plasticity model. *Computer Methods in Applied Mechanics and Engineering* 2012; **237**–**240**:1–9.
47. Hughes TJR, Winget J. Finite rotation effects in numerical integration of rate constitutive equations arising in large-deformation analysis. *International Journal for Numerical Methods in Engineering* 1980; **15**(12):1862–1867.
48. Flanagan DP, Taylor LM. An accurate numerical algorithm for stress integration with finite rotations. *Computer Methods in Applied Mechanics and Engineering* 1987; **62**:305–320.
49. Scherzinger WM, Dohrmann CR. A robust algorithm for finding the eigenvalues and eigenvectors of 3x3 symmetric matrices. *Computer Methods in Applied Mechanics and Engineering* 2008; **197**:4007–4015.
50. Qidwai MA, Lagoudas DC. On thermomechanics and transformation surfaces of polycrystalline NiTi shape memory alloy material. *International Journal of Plasticity* 2000; **16**:1309–1343.
51. Armero F, Pérez-Foguet A. On the formulation of closest-point projection algorithms in elastoplasticity – part I: The variational structure. *International Journal for Numerical Methods in Engineering* 2002; **53**:297–329.
52. Simo JC, Taylor RL. Consistent tangent operators for rate-independent elastoplasticity. *Computer Methods in Applied Mechanics and Engineering* 1985; **48**:101–118.
53. Pérez-Foguet A, Rodríguez-Ferran A, Huerta A. Consistent tangent matrices for substepping schemes. *Computer Methods in Applied Mechanics and Engineering* 2001; **190**:4627–4647.
54. Graf A, Hosford W. Calculations of forming limit diagrams. *Metallurgical Transactions A* 1990; **21A**:87–94.